SEISMIC MODELLING OF EARTH STRUCTURE (1996)
Eds. Enzo Boschi, Göran Ekström and Andrea Morelli

5

Construction of synthetics for 2D structures; core phases

DON V. HELMBERGER, LIAN-SHE ZHAO and ED GARNERO
Seismological Laboratory, California Institute of Technology, Pasadena, CA 91125, U.S.A.

5.1 Introduction

Recent studies have emphasized the prominence of anomalous high and low velocity regions in the lower mantle. For example, slower than average seismic shear wave velocities beneath the central Pacific accompanied by surrounding higher than average velocities is common to most tomographic studies (*e.g.*, see Tanimoto, 1990; Masters *et al.*, 1992; Su and Dziewonski, 1994). Images from these reports indicate long wavelength (>3000 km) structures with velocity anomalies of up to ±2.5%. A particularly prominent slow region occurs just north of the Fiji-Tonga region in all of these models and has been noted by many authors with respect to differential times of body waves, such as ScS-S by Sipkin and Jordan (1980), S-SKS by Garnero and Helmberger (1993) and others. The latter study demonstrates that S-SKS time predictions made from present 3D models do not agree with all of the observations. Since this anomaly may well be associated with up-welling currents in the mantle, the seismic details become particularly important especially at the shorter wavelengths associated with body waves (5-100 km). Thus, better methods of generating realistic synthetics for these types of complex models would be useful and are addressed in this study.

One of the most commonly used methods of generating body wave synthetics is due to Chapman (1976), called the WKBJ method or WKB. This method is discussed and tested in a review paper, Chapman and Orcutt (1985) for 1D layered earth models, including core-phases. Generalizations of this method to 2D and 3D are given by Chapman and Drummond (1982) and Frazer and Phinney (1980), respectively. The first of these proved very useful in modeling multi-bounce shear waves (see Helmberger *et al.*, 1985; and Graves and Helmberger, 1988). The latter 3D method requires some modifications as proposed by Burdick and Salvado (1986). Moreover, they demonstrate that the usual WKB method of using rays

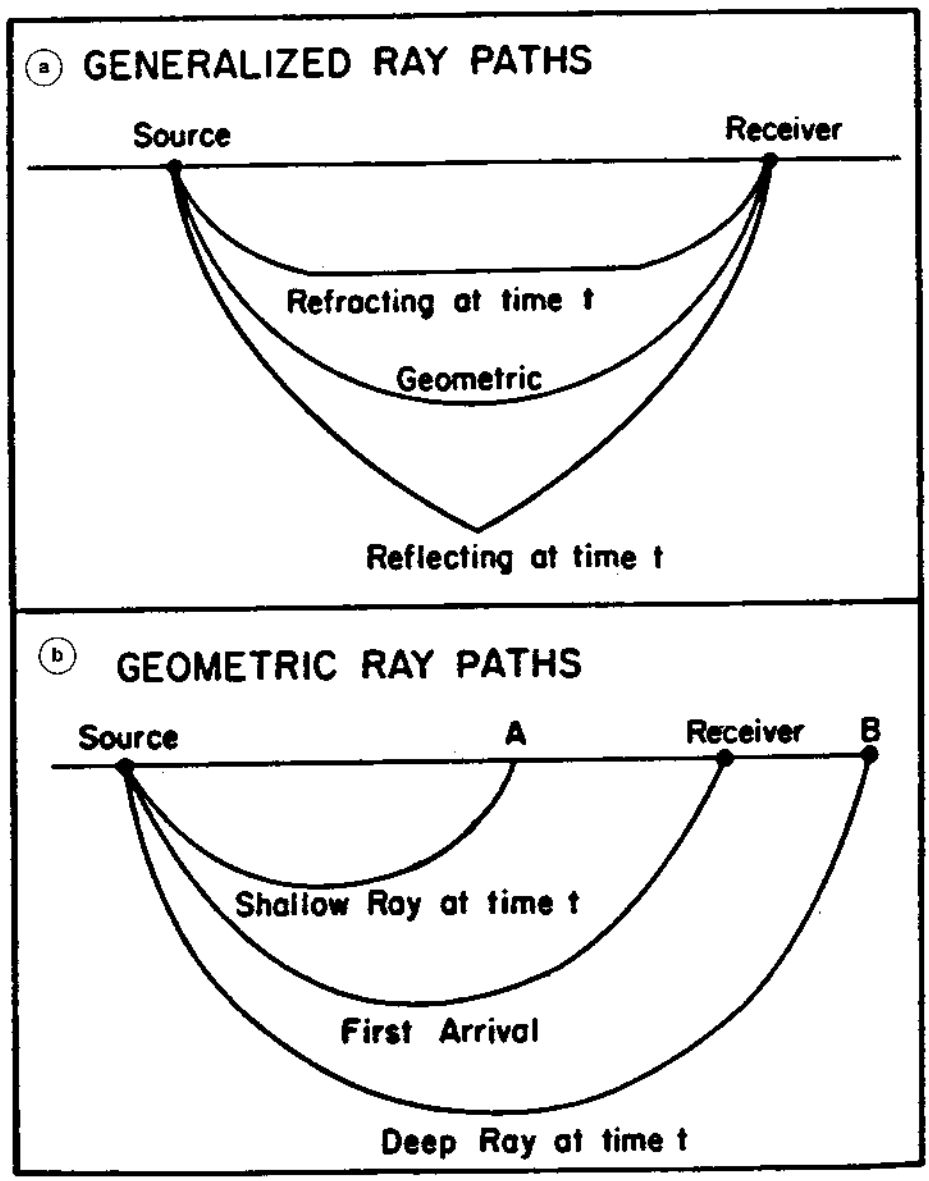

Figure 5.1a,b Two displays of ray paths that are commonly used in generating synthetics. (a) it shows the non-Fermat type of rays used in Cagniard-de Hoop theory; (b) it shows the geometric rays used in WKB theory, modified from Burdick and Salvado (1986).

that under-shoot and over-shoot the receiver can easily violate casuality and suggested that the earlier methods of Chapman (1974) that only allow ray paths that arrive at the receiver are probably more accurate in 2D modeling, see Figure 5.1a,b.

Figure 5.1b illustrates the ray paths normally associated with the WKB method. In this case, the phase function is defined by

$$t = T(p) - p\,[X(p) - x] \tag{5.1}$$

where $T(p)$ and $X(p)$ are the times and ranges associated with p, the geometric ray parameter. The first arrival occurs when $X(p) = x$ where x is the receiver distance. The amplitude of the arrival is controlled by $1/(X(p)-x)$. This function has a square-root singularity at $X(p) = x$ and is equal to $(\delta p/\delta t)$ where δp and δt are differentials associated with the family of rays arriving in the neighborhood of x.

The ray paths displayed in the Figure 5.1a are non-Fermat paths, Chapman and Drummond (1982), and are basically generalized ray paths for a finely layered model. They correspond to rays that reflect from each interface such that they arrive at the source and receiver. The wave-field in terms of generalized rays can be approximated by summing the primary rays only;

$$\phi = \sqrt{\frac{2}{x}}\frac{1}{\pi}\left[\frac{1}{\sqrt{t}} * \left(\sum_j \mathrm{Im}\,\frac{\sqrt{p}}{\eta_1}\,\Pi(p)\,\frac{dp}{dt_j}\right)\right] \tag{5.2}$$

where $\Pi(p)$ contains the product of reflection and transmission coefficients. The function $\dfrac{dp}{dt}$ is obtained from

$$t = px + 2\sum_{j=1}^{n} Th_j\,\eta_j \tag{5.3}$$

where $p(t)$ forms the complex contours, $\eta_j = \left(\dfrac{1}{\alpha_j^2} - p^2\right)^{1/2}$, see Helmberger (1983). The layer thicknesses are given by Th_j and velocities by α_j. Note that for each interface, we must determine a $p = p_0$ and associated t_0 which describes a path connecting that interface t_0 the source and receiver satisfying Snell's law. Wiggins and Madrid (1974) demonstrated by numerical experiments that when the structure is smooth, one can approximate the contribution from each generalized ray by $(\delta p_0/\delta t_0)_j$. That is, we can replace the complex evaluation of the expression inside the parenthesis of eq. (5.2) by a real function, namely,

$$\sum_j \frac{\delta p_0\,(j-1,j)}{\delta t_0\,(j-1,j)} = \sum_j \mathrm{Im}\,\frac{\sqrt{p}}{\eta_1}\,\Pi(p)\,\frac{dp}{dt}\,. \tag{5.4}$$

They called this approximation quantized ray theory which was later generalized to disk ray theory, Wiggins (1976). Chapman (1974) derived this result theoretically by replacing the generalized ray summation by a complex ray parameter integration over depth. The first-motion approximation of this integral yields again the $[X(p) - x]$ singularity and the $(\delta p_0/\delta t_0)_j$ behavior. We will, henceforth, call this approximation WKM since the solution is so similar to that of WKB but to distinguish the ray paths involved in its implementation.

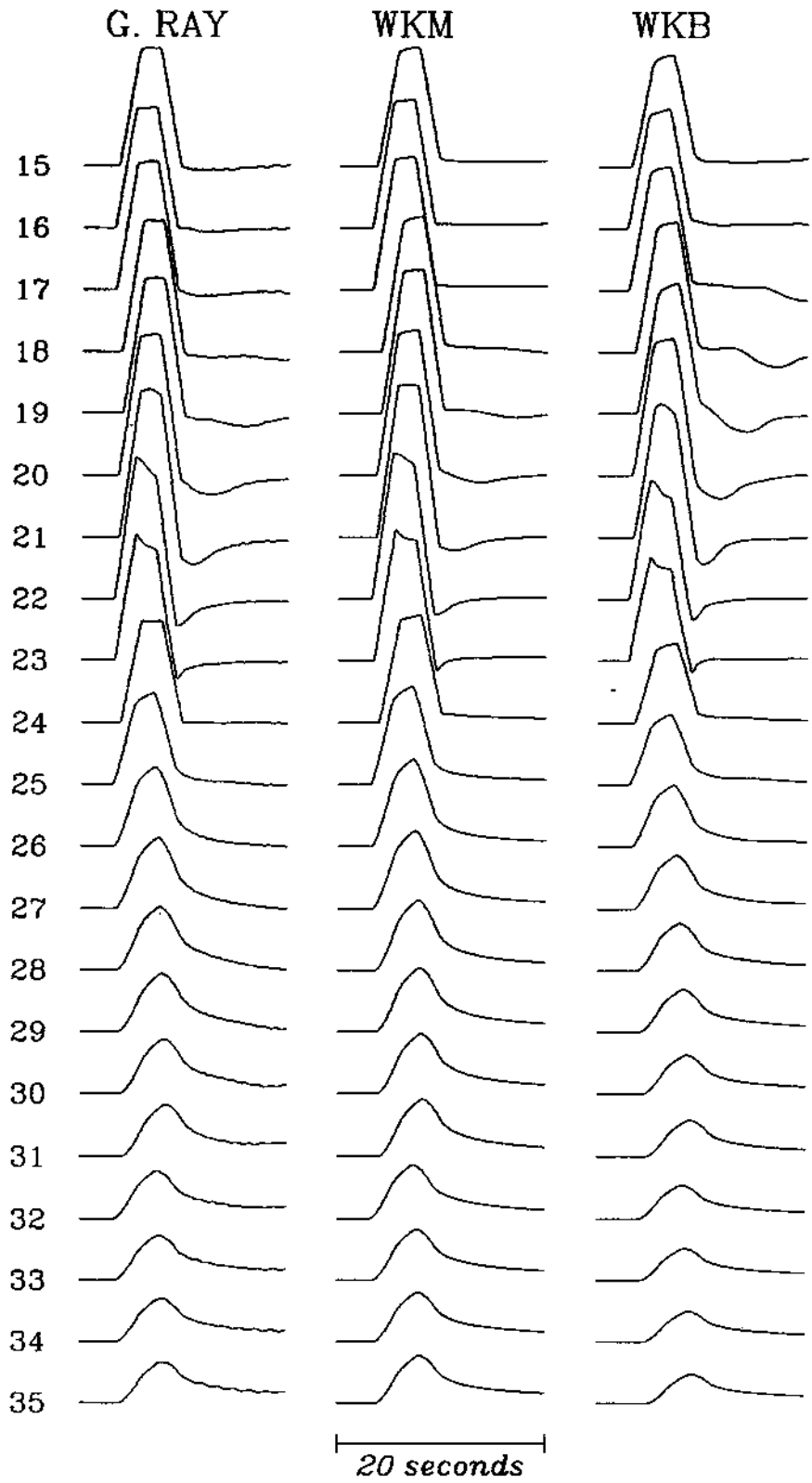

Figure 5.2 Comparison of synthetics generated by GRT, WKM, and WKB. Distances denoted in degrees are given on the left. The diffraction starts at 24° where the waveforms begin losing their high frequency energy.

In Figure 5.2, we display the synthetics generated from these methods to show their compatibility. The model is given in Figure 5.3 which consists of a linear gradient over a halfspace. The synthetics from the three methods are normalized in amplitude to the GRT results at the range of 15°, and thus the amplitude decay with distance reflects the approach of the geometric shadow. This shadow is at 24° and, as expected, the amplitudes should be about half their values away from shadow. The (t) vs. (p) curve derived from the WKB approach, see Figure 5.4, ends at the geometric ray, since rays with smaller p's do not return to the surface. Thus, half of the $(\delta p/\delta t)$ curve produces half of the amplitude. At smaller distances, more of the curve is developed and the amplitude grows; however, the well-known truncation phase causes some distortions in the waveform.

The ray paths associated with the WKM method for the situation where the receiver is situated at the shadow boundary are included in Figure 5.3. Note that even though the velocity is constant in the lower halfspace, we still impose a uniform layered structure. The (t) vs. (p) curve formed by plotting the p_0's and t_0's, see Figure 5.4, are identical to those using WKB, but they have the extended portion into the shadow included by the dotted line. This extension tends to reduce the truncation phase and produces better fits to the GRT results which handles the diffraction effects.

Wiggins (1976) suggested that a particularly useful approach is to use disk ray theory for the smooth portions of models and GRT for large velocity jumps and for diffracted phases where complex ray parameters are involved. This will be the approach followed in this paper where we will rely on the 2D modifications of the GRT method to test WKM solutions where possible. In the next section, we will introduce the local Earth stretching approximation and test it against the finite-

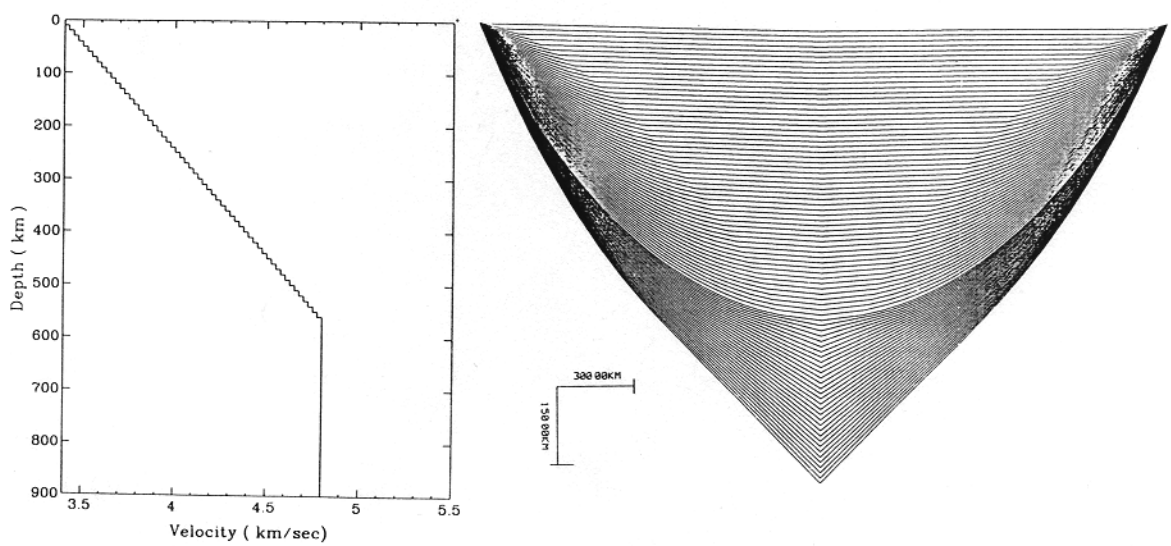

Figure 5.3 A *S*-velocity model displaying a linear gradient, approximated by layers, is given on the left. On the right are displayed the various ray paths connecting the source to the receiver while reflecting from each interface. This particular distance, 24°, is at the shadow zone boundary.

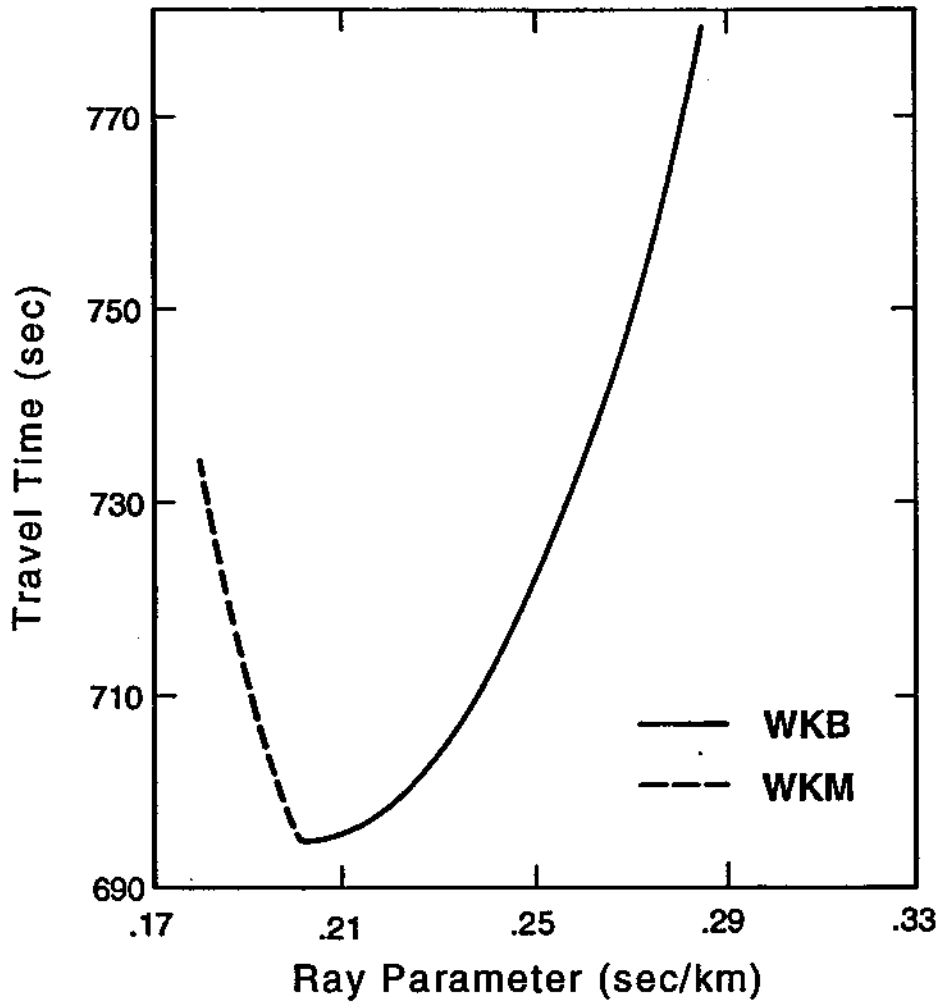

Figure 5.4 Comparison of p (s/km): t (s) curves generated by WKB and WKM.

difference method assuming local crustal models. Next, we discuss comparisons of observations of various lower mantle and core phases against 1D synthetics. This will be followed by the construction of synthetics of core phases for possible 2D structures.

5.2 Review of GRT theory and local stretching

Although GRT for parallel interfaces has been well developed, the modifications for nonplanar structure have received less attention as reported on recently by Richards *et al.* (1991). In this report we are particularly interested in models with many layers where the travel times are relatively large compared to signal duration. This condition allows still greater approximations which leads to faster computations. We begin with a brief review of the theory developed for locally dipping interfaces, see Helmberger *et al.* (1985). The problem setup is given in

Figure 5.5. The solution in terms of generalized rays becomes

$$\phi(r, t) = \sqrt{\frac{2}{r}}\frac{1}{\pi}\left[\frac{1}{\sqrt{t}} * \partial m\left(\frac{\sqrt{p_1}}{\eta_1}\frac{dp}{dt} T_{12}(p_1)\, T_{23}(p_2)\right)\right] \tag{5.5}$$

for the displacement potential describing the direct arrival, where T_{ij} are the transmission coefficients. The derivative (dp/dt) is obtained from the Cagniard-de Hoop contour, $p(t)$, defined by $t = (p_i d_i + \eta_i h_i)$, where we sum over i.

The derivative of t becomes $\dfrac{dt}{dp} = \left(d_i - \dfrac{h_i p_i}{\eta_i}\right) = 0$ if $p_i = \dfrac{\sin\theta_i}{\beta_i}$ and $\eta_i = \dfrac{\cos\theta_i}{\beta_i}$,

where β_i is the local velocity and $\eta_i = \left(\dfrac{1}{\beta_i^2} - p_i^2\right)^{1/2}$.

We denote this $p_i = p_{i0}$ which corresponds to Snell's law where the ray parameter, p, is locally adjusted for dipping structure.

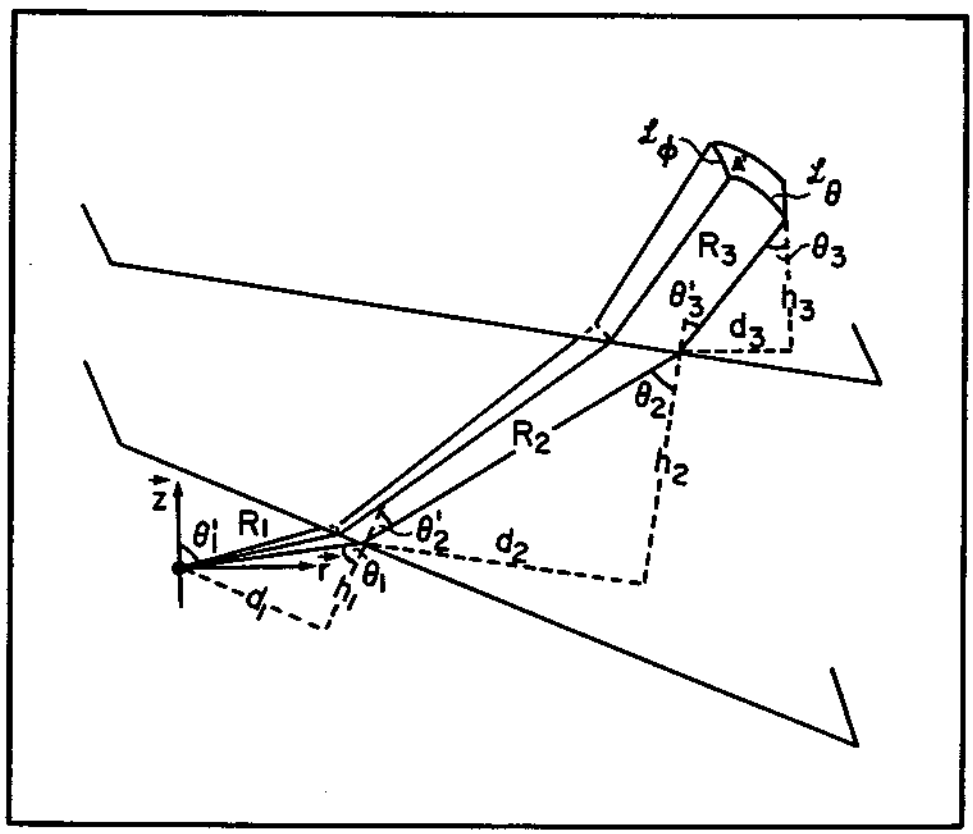

Figure 5.5 Display of ray path through a dipping structure and associated coordinates used in Cagniard-de Hoop formalism, after Hong and Helmberger (1978).

The corresponding arrival time, t_0, becomes $t_0 = \frac{\sin\theta_i}{\beta_i} d_i + \frac{\cos\theta_i}{\beta_i} h_i = \frac{R_i}{\beta_i} = t_{i0}$ as is apparent in Figure 5.5. The factor (dp/dt) becomes complex for real values of p greater than $p_i = p_{i0}$ etc., where the imaginary part of p is the same for each ray segment. Thus, we need to evaluate each transmission coefficient $T(p_i)$ for its local complex ray parameter. Synthetics generated with this theory compare very well with finite-difference calculations as discussed in Vidale *et al.* (1985) and Helmberger *et al.* (1985). However, this procedure is cumbersome in the same way as computing synthetics in spherical shells, since the interfaces are not parallel (see Gilbert and Helmberger, 1972). In this case, the solution was simplified by adjusting the velocities to correct for changes in the relative slopes of interfaces which leads to earth flattening.

We can apply the same idea here, which we call the local stretching approximation. In the above parameter space p_i, we have d_i, β_i, h_i and we want to transform to d_i', β_i', h_i' where $p_i = p$, a constant along the ray path. The new d's are along the interfaces and the h's become the vertical separations between interfaces. The three equations needed to produce this mapping are:

(1) $t_i = t_{i0}$, conservation of travel time

(2) $dt/dp = 0$, $p_0 = p_{i0}$, Snell's law (5.6)

(3) $d^2t/dp^2\ (d_i', \beta_i', h_i') = d^2t/dp^2\ (d_i, \beta_i, h_i)$, conservation of geometric amplitude, see Helmberger *et al.* (1985) for details. Explicitly, the second derivative is easily derived from dt/dp, namely

$$\frac{d^2t}{dp^2} = -h_i / \beta_i^2 \eta_i^3 .$$

These three equations are easily solved to obtain:

$$\beta_i' = (\eta_i^2 - p_0^2)^{-1/2} \quad \text{or} \quad \eta_i' = \eta_i \tag{5.7}$$

$$h_i' = (\beta_i')^2 \eta_i\, t_{i0} \tag{5.8}$$

and

$$d_i' = (\beta_i')^2 p_0\, t_{i0} \tag{5.9}$$

per segment of ray path.

Geometrically, this transformation has a very simple form, namely, (5.7) becomes $R_i / \beta_i = R_i' / \beta_i'$, see Figure 5.5. Expression (5.8) becomes $h_i' = \cos\theta_i R_i'$ and (5.9) yields $d_i' = \sin\theta_i' R_i'$. Thus, the ray paths displayed in Figure 5.5 map into a flat-layered model with d_i's lying along the layers and h_i's perpendicular to the layers. Note that if a ray is reflected back through the layering in Figure 5.5, it would transform into a layered stack different from the first pass, etc. In this fash-

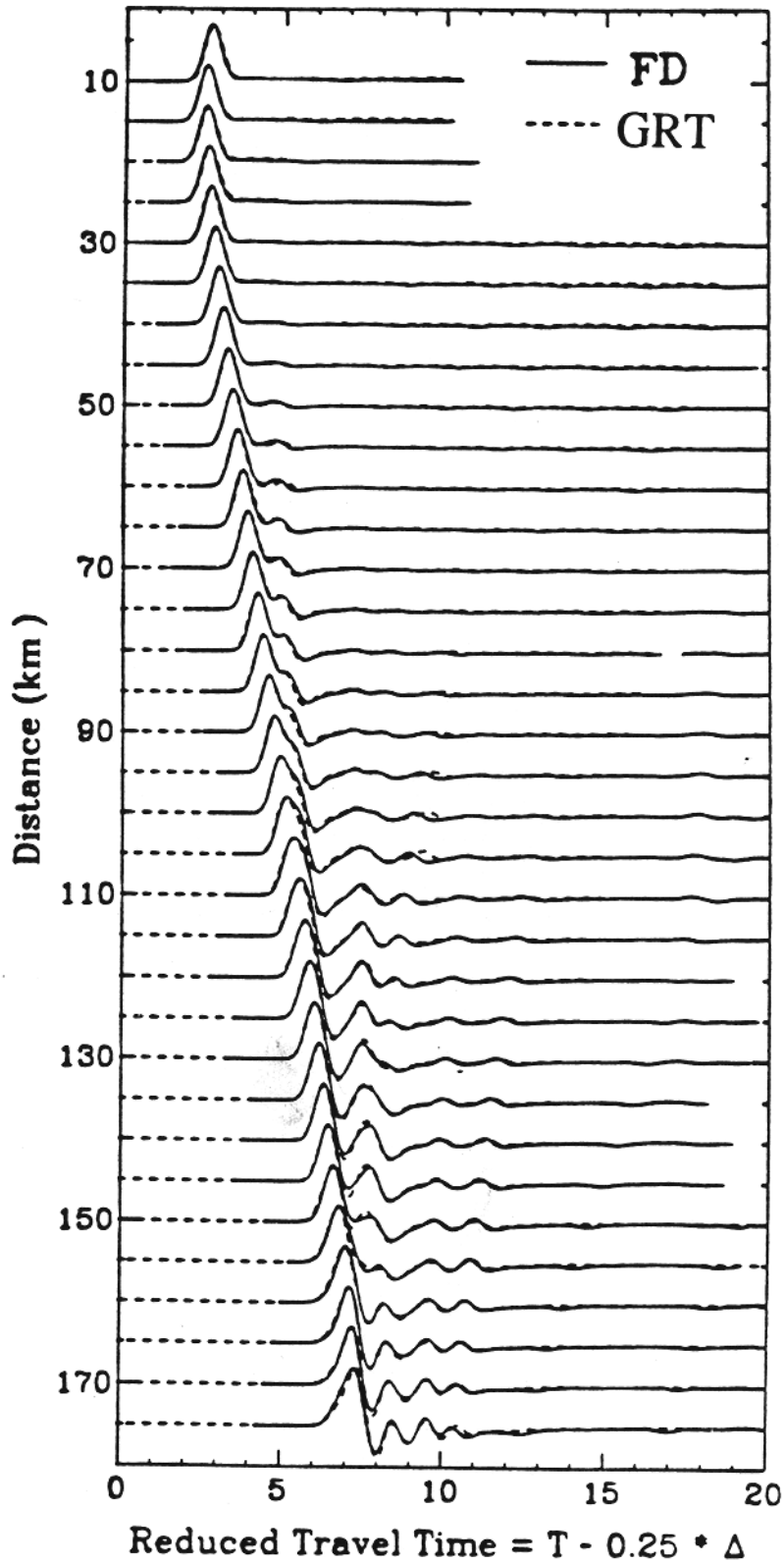

Figure 5.6 Comparison of theoretical displacements generated by finite-difference versus modified Cagniard-de Hoop codes. The model parameters are given in Table 5.1 and the lateral variation displayed in Figure 5.7.

ion, head waves can develop above the source and locally trapped waves are possible, see Helmberger *et al.* (1985). But, since this transformation is path-dependent, it must be done for every ray path which makes it less convenient than earth stretching.

One of the most definitive tests of any approximate analytical method is to test predictions against a numerical method such as finite-difference. However, such tests are only practical at local distances where the travel time to source duration is not too large and the grid-size remains manageable. The results for a 2D crustal model are presented in Figure 5.6, where we have assumed a strike-slip point source at a depth of 10 km. Figure 5.7 displays the model variation along with a ray path before and after the transformation, and the model is given in Table 5.1. The numerical method of interfacing earthquake sources with finite-difference is discussed in Helmberger and Vidale (1988). Since surface waves tend to dominate the waveforms, we have set the velocities in the upper halfspace to those in the surface layer. This assumption then allows the comparison between the direct arrival and lower crustal triplications to be enhanced and a meaningful comparison between the methods made with the surface waves removed. The comparison of synthetics is very good for the distances covering the cross-over of direct *S* to diving *S*. We have conducted a number of similar tests both against finite-difference and linearly dipping GRT that give satisfactory results. These results will be presented in a later study on modeling 2D regional phases.

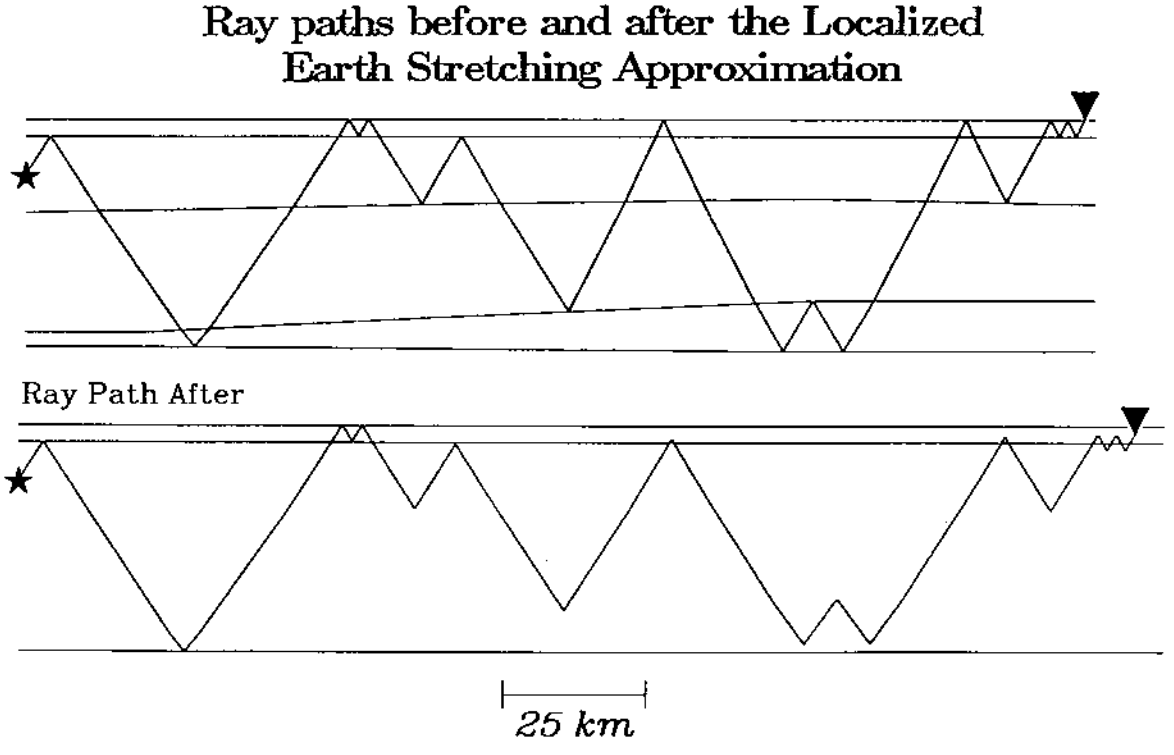

Figure 5.7 Example of ray path before and after local stretching.

Table 5.1. Crustal model.

Layer	*S*-velocity (km/s)	Density (gr/cc)	Thickness (km)
1	3.3	2.6	3
2	3.5	2.7	14
3	3.7	2.75	20.5
4	3.9	2.9	2.5
5	4.6	3.3	∞

In the remaining sections of this paper, we will be concerned with constructing 2D synthetics involving lateral variation at the base of the mantle, D″. At present there is considerable uncertainty about the detailed structure of this transitional layer, see Weber and Davis (1990). However, there is general agreement that it must be laterally varying. For example, a recent paper by Kendall and Shearer (1993) presents a preliminary global map of thicknesses which ranges from 100 to 400 km. For the Central Pacific region, Garnero *et al.* (1993a) suggest that the thickness of D″ may vary and may thin out from the surrounding regions to a thickness of 180 km. Thus our first example set of synthetics will address a linear transition zone from a thick D″ layer to a thin one, and will include the effects on the SKS-S crossover. This will be followed by the effects on SmKS, [*S*-waves in the mantle and *P*-waves in the core that reflect (m-1) times on the underside of the CMB] due to a low velocity anomaly situated at the base of the mantle. A third section treats the effects on SPdKS; that is SKS waves that couple with segments of *P*-diffraction along the top of the CMB.

5.3 D″ structure and lower mantle triplications

We begin by reviewing some progress made in modeling SH and SV observations in the cross-over ranges from *S* to SKS in one region; namely, paths from South America to the U.S. A comparison of synthetics with observations across this interesting set of distances is given in Figure 5.8, taken from a study by Lay and Helmberger (1983). The upper set of synthetics correspond to a D″ model SLHO containing a first-order increase in *Vs* (3%) at a depth of 2600 km. The bottom set of synthetics corresponds to a similar model SLHO-SV except it contains a thin high velocity layer (5% jump in a layer 20 km thick) at the CMB and a slightly perturbed outer core model, see the above reference.

The theoretical GRT response for the latter model is displayed in Figure 5.9 along with LP WWSSN synthetics. We have plotted the step response here to emphasize the differences in frequency content between the various arrivals which is suppressed by the effects of the long period instrument response. Note that the phase ScS(SV) is negative relative to *S*, but in these responses a small positive spike occurring slightly ahead of ScS(SV) is observable. This arrival is the *S*-wave

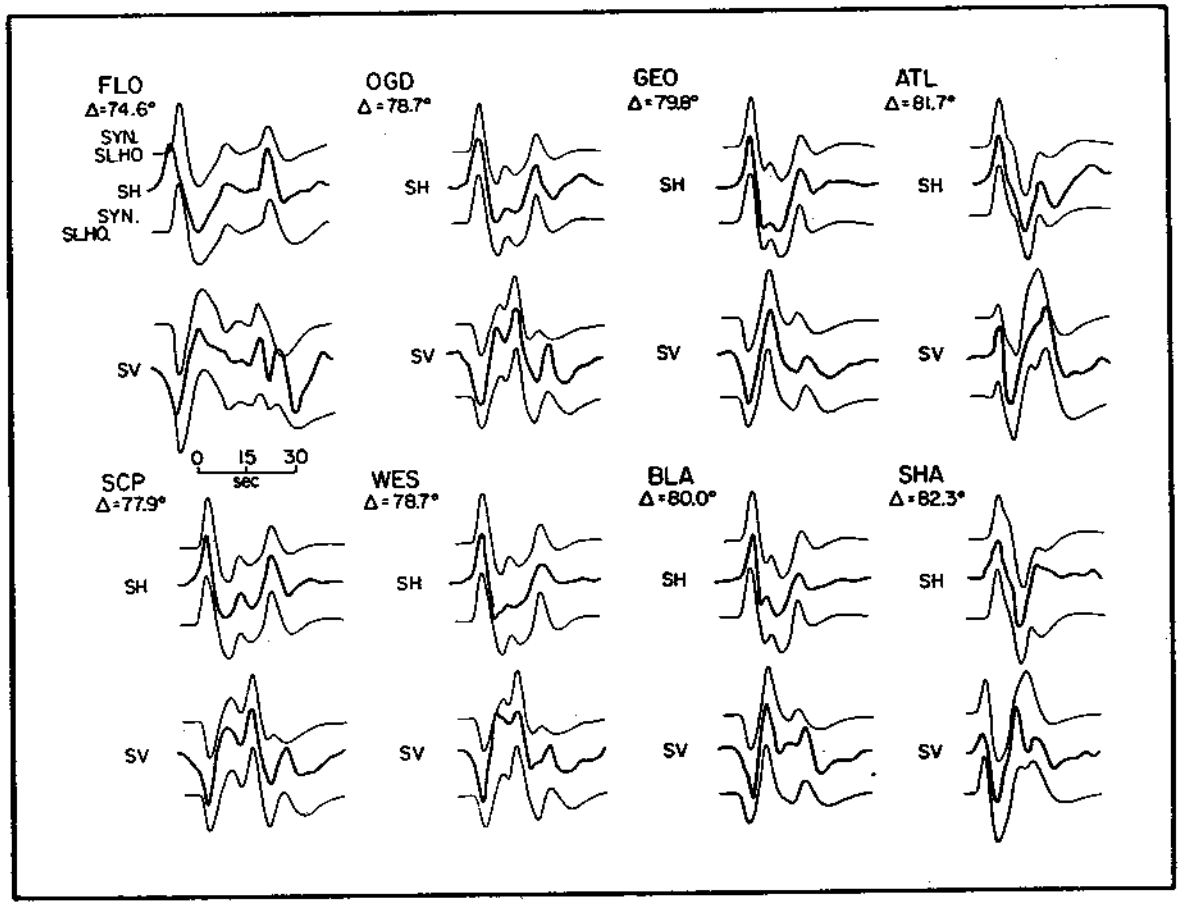

Figure 5.8 Comparison of synthetics, with data showing the (SKS-S) cross-over. (After Lay and Helmberger, 1983), see Figure 5.9 for phase identification.

produced by the thin layer which has positive polarity for (SV). The same phase can be seen in the SH response but since it has the same polarity as ScS it becomes less noticeable. Such a thin layer can explain the apparent shift in timing of ScS (SV) versus (SH) as first described by Mitchell and Helmberger (1973) for similar paths. Of course, a similar feature could be produced by anisotropy. At the largest range, 82.3°, one can see the SV-phases *S* and ScS approach each other which makes the core-diffracted SV disappear rapidly, especially at larger ranges.

With the installation of TERRAscope and the Berkeley broadband seismographic network, we should see some excellent broadband record sections through the cross-over in the future. Profiles of SH and SV obtained from these records are displayed in Figures 5.10a and 5.10b respectively. We have included 1D predictions from a model proposed by Zhang and Lay (1984) and a new model by Ding and Helmberger (1995). These models are displayed in Figure 5.11. Although there are some interesting mismatch in these comparisons, the fits on average are quite good. We have not observed a good set of records from Fiji to date, but we would expect a much more interesting section based on the results

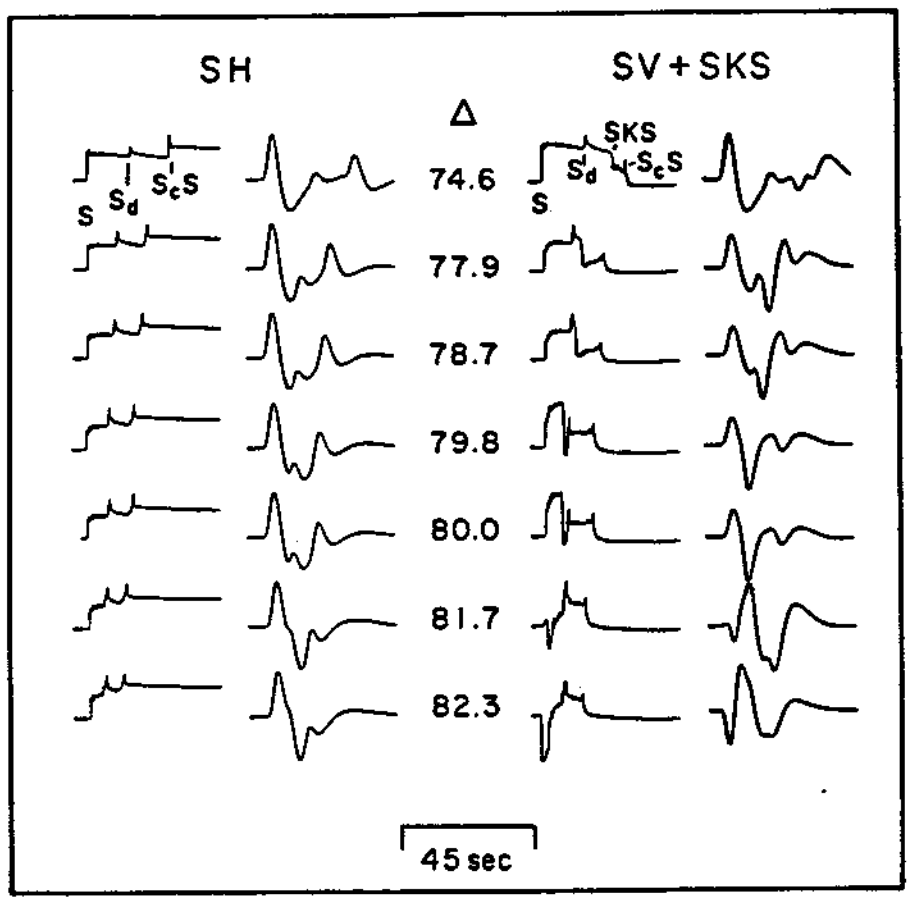

Figure 5.9 Synthetic step responses for model SLHO-SV (see Lay and Helmberger, 1983) and synthetics for SH on the left and SV on the right.

of Garnero *et al.* (1988). With this in mind, we will consider an arbitrary model that changes from one type of structure to another.

Synthetics appropriate for broadband instruments assuming a similar Lay-type model, SYL1 of Young and Lay (1987), are displayed in Figures 5.12a-d and 5.13a-d along with 2D record sections. The SYL1 model is displayed on the left in Figure 5.14, with the transition to a very thin D″ model given on the right. The source depth is 565 km, a depth appropriate for deep events. The middle panel of Figure 5.14 displays the iso-velocity boundaries along with a sample of WKM rays. Each of these ray paths are stretched and fed to a slightly modified 1D Cagniard-de Hoop code which approximates the density and Poisson's ratio from empirical relationships.

Figure 5.12a shows most of the D″ triplication where the S_d-arrival from D″ over-takes the slightly slower *S* near 88°. At ranges larger than 96° these two pulses (S_d and ScS) join asymptotically. The D″ triplication can also be seen in SV, Figure 5.13a, where the cross-over occurs near 88°. Note that again *S* and S_d dominate beyond 94° where now ScS is negative as in Figure 5.9.

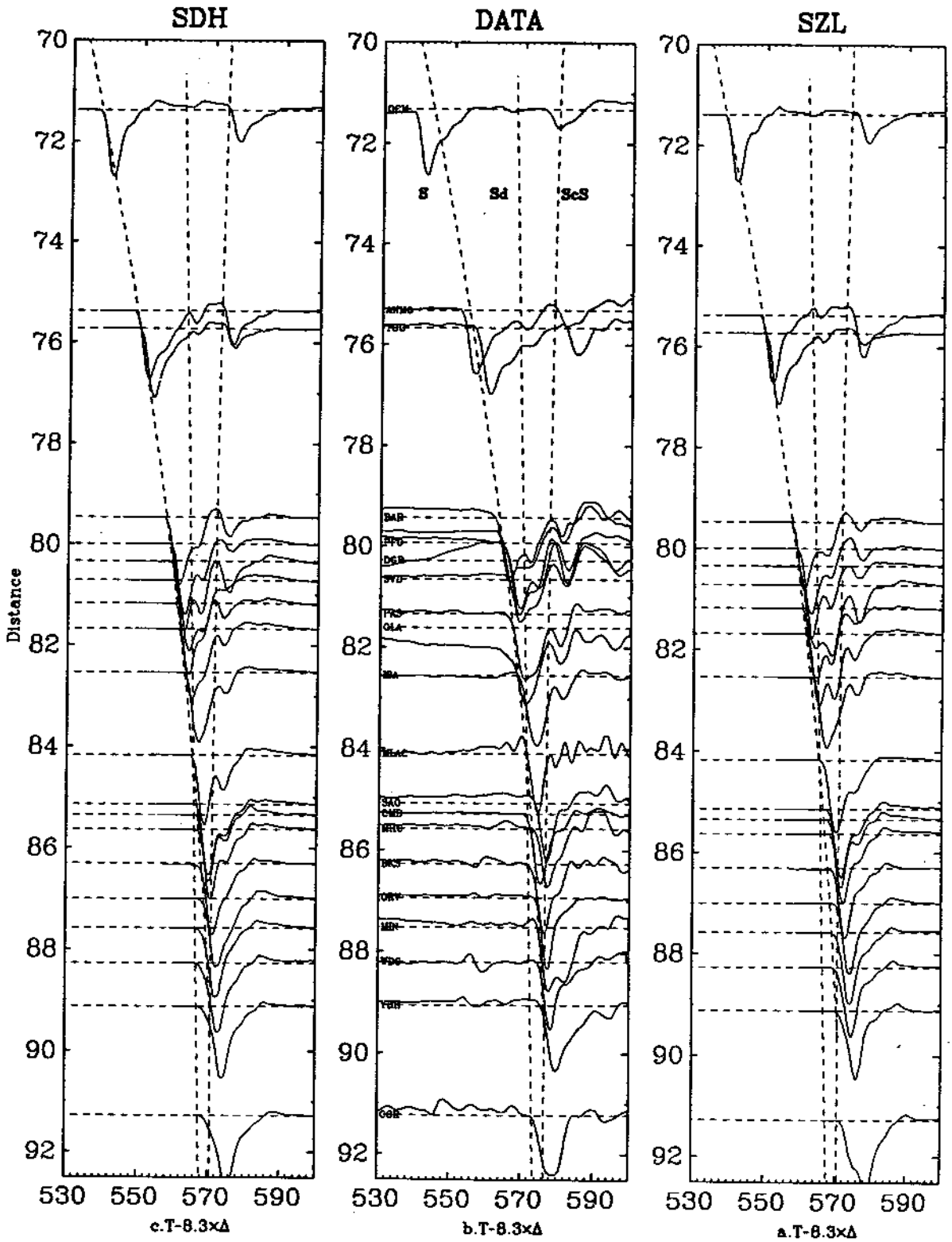

Figure 5.10a The dotted lines indicate the arrival times of S, S_d, and ScS calculated from the SDH model. These lines are delayed 6 s in the DATA section to account for the expected upper mantle delays beneath the Western United States, TNA of Grand and Helmberger (1984).

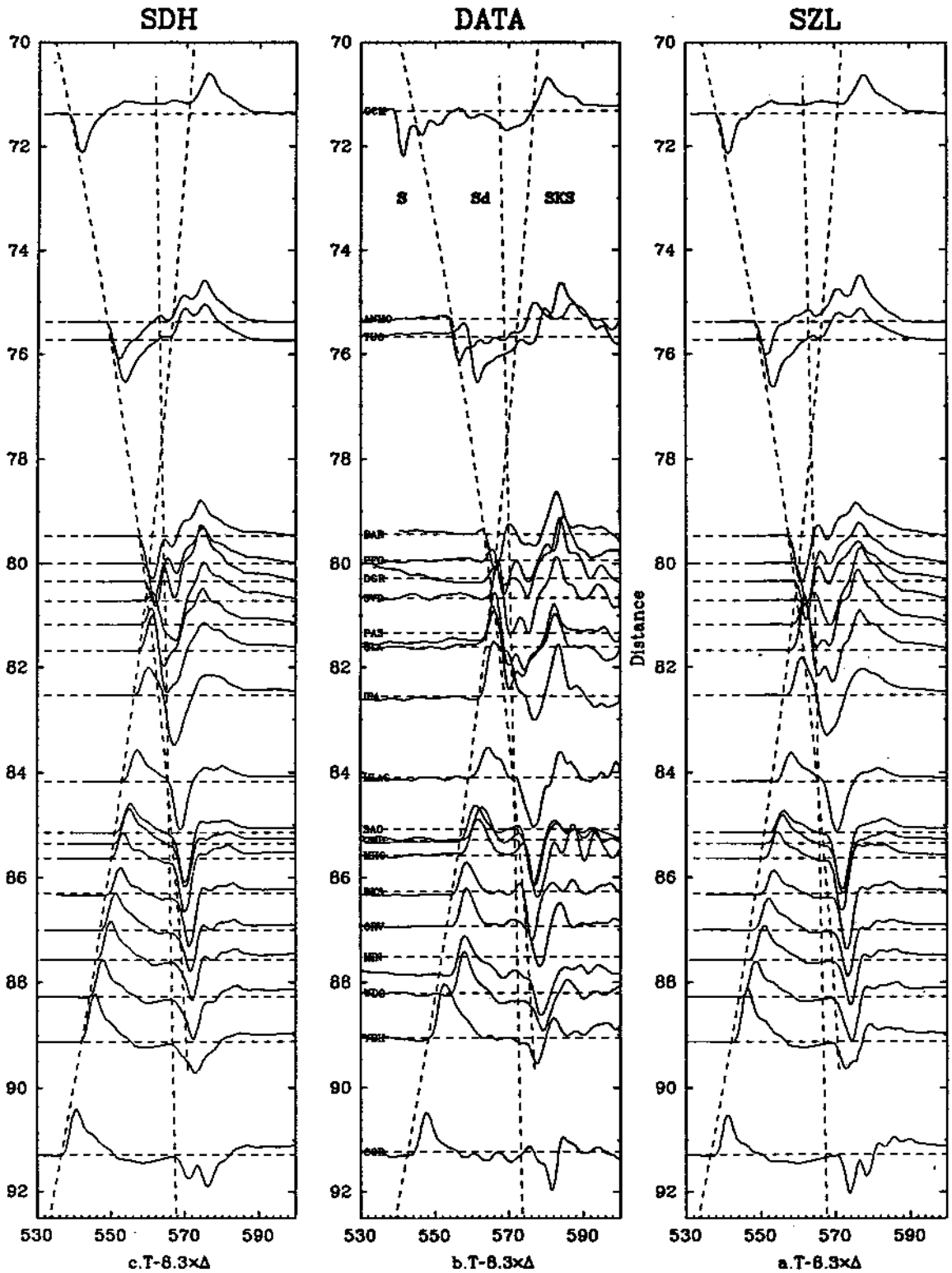

Figure 5.10b The dotted lines indicate the arrival times of S, S_d, and SKS. The ScS arrival is the same as in Figure 5.10a. Some large secondary arrivals, roughly 20 s behind S, occur in similar record sections at smaller epicentral distances at some of the stations, *i.e.*, BAR, and is presumably crustal-coupled PL waves caused by complex crustal structures, see Ding and Helmberger (1995).

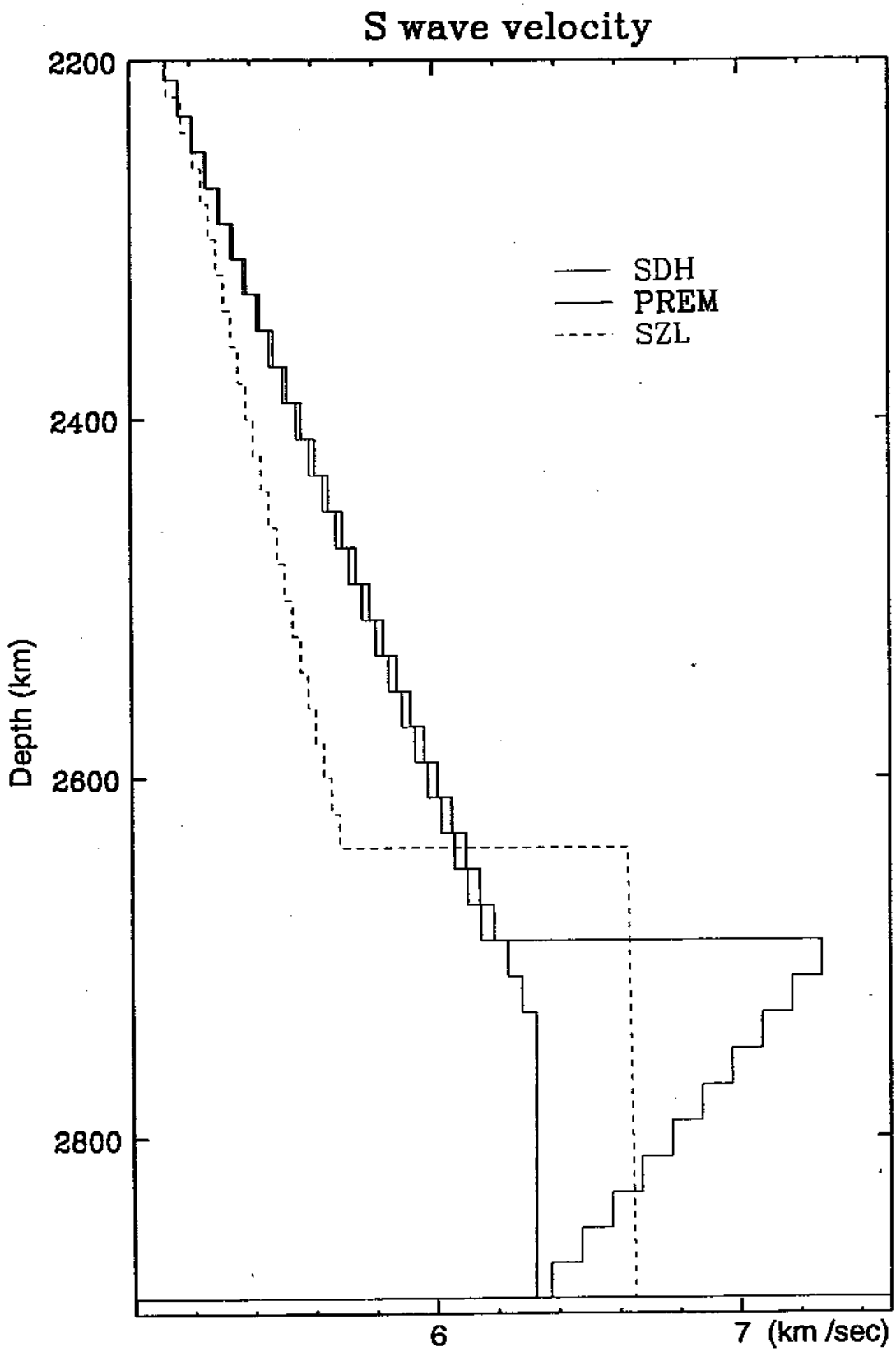

Figure 5.11 Plots of three 1D plots, PREM (Dziewonski and Anderson, 1981), SZL (Zhang and Lay, 1984), and SDH (Ding and Helmberger, 1995).

Panels (b), (c) and (d) in Figures 5.12 and 5.13 correspond to various positioning of the source where the ray paths encounter the 2D portion of the model. Rays sample the average structure when the source is situated about 1000 km to the left of the 2D edge, see Figure 5.14. This source position produces the synthetics in panel (c). The other two panels correspond to source shifts relative to this position; namely, 3000 km to the left in (b) and 3000 km to the right in (d). Thus, we would expect (b) to be similar to (a) and (d) to be the simplest of all since the right-hand model in Figure 5.11 is nearly a PREM-type model (Dziewonski and Anderson 1981). Indeed, the synthetics in Figures 5.12d and 5.13d are relatively simple except for the small complication caused by the thin basal layer which is expected, as with the model for the South American region. The *S* arrival from this thin layer becomes the first arrival at the largest distance, see Figure 5.12d, at 96°. Panel (c) is also relatively simple to interpret. The thin layer no longer dominates the D″ arrivals and a more normal S_d phase begins to develop but remains a secondary arrival. The synthetics in panel (b) are the most complicated both in nature and in computation. For example, it was not possible to find ray paths between the source and receiver for some of the layers in D″ at the three largest ranges. This means that the S_d phase is weaker and more energy is transmitted downward than in the other cases. Some of this energy reappears in late arriving ScS, but such a feature is highly dependent on the details of the lateral variation.

One of the reasons for suggesting a model like that displayed on the right in Figure 5.14 was the anomalies in differential *S*-SKS times at ranges 84° to 96° from Fiji-Tonga events relative to the South American events, see Garnero *et al.* (1988). These observed differential times vary considerably for various paths, Garnero *et al.* (1993a), but are bracketed by the predicted times going from panel (a) to panel (d). The actual *S*-SKS cross-over was never observed because of the lack of California stations and poor source-station geometry. The installation of TERRAscope and the Berkeley net has changed this situation and a few recent events have been recorded showing this cross-over and will be reported on shortly.

5.4 Modeling outer-core phases

The use of synthetic seismograms in the interpretation of core-phases, namely the SKS family, has been active since Kind and Müller (1975) and Choy (1977). These papers developed the basic understanding of the wave-propagation involved. The first of these introduced the applications of reflectivity while the latter treatment was more theoretical, the so called full-wave theory. The comparison of synthetics generated by these two methods is discussed in Choy *et al.* (1980) where they conclude that the comparisons of synthetics generated by different methods tend to agree among themselves much better than the comparison of data with synthetics generated from existing models.

We will begin this section with a comparison of observations against 1D synthetics. These comparisons will serve to highlight the usefulness of 1D modeling

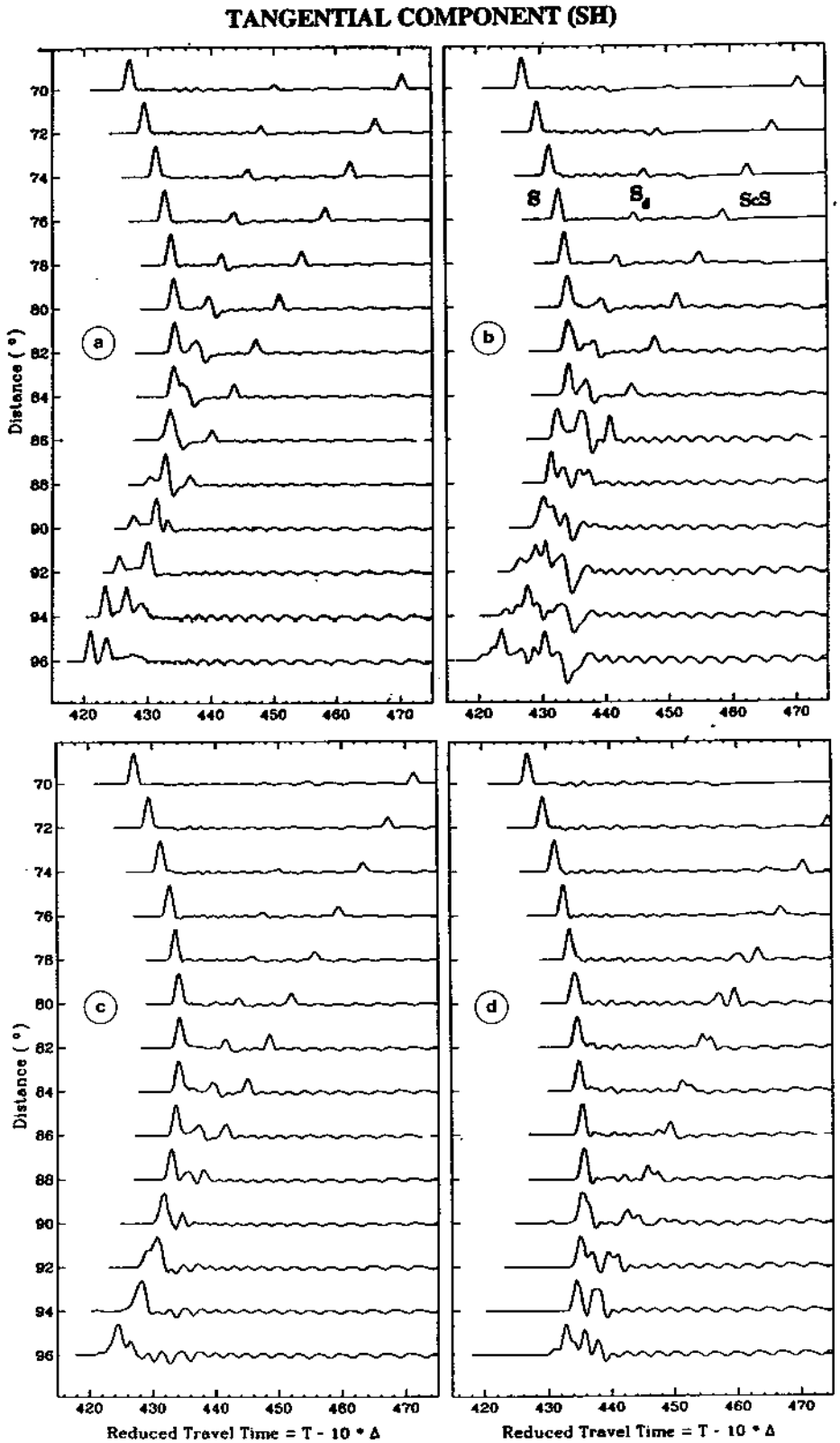

Figure 5.12a-d Four panels of SH synthetics are presented with (a) a pure-path SYL1 model, Young and Lay (1987). Panels (b), (c) and (d) correspond to various positions of the source along the 2D section presented in Figure 5.14, going from left to right.

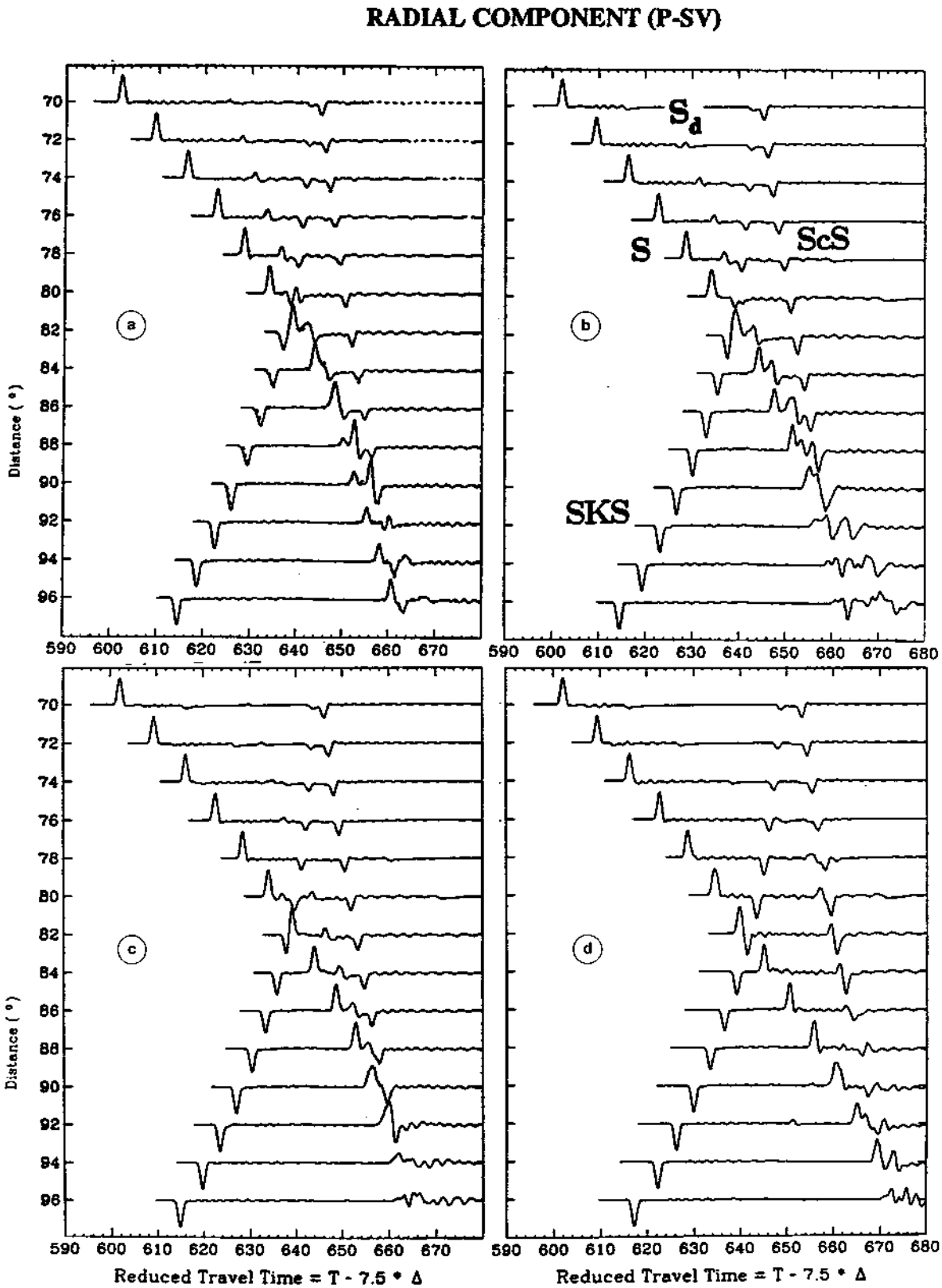

Figure 5.13a-d Corresponding SV synthetics displaying the cross-over from *S* to SKS.

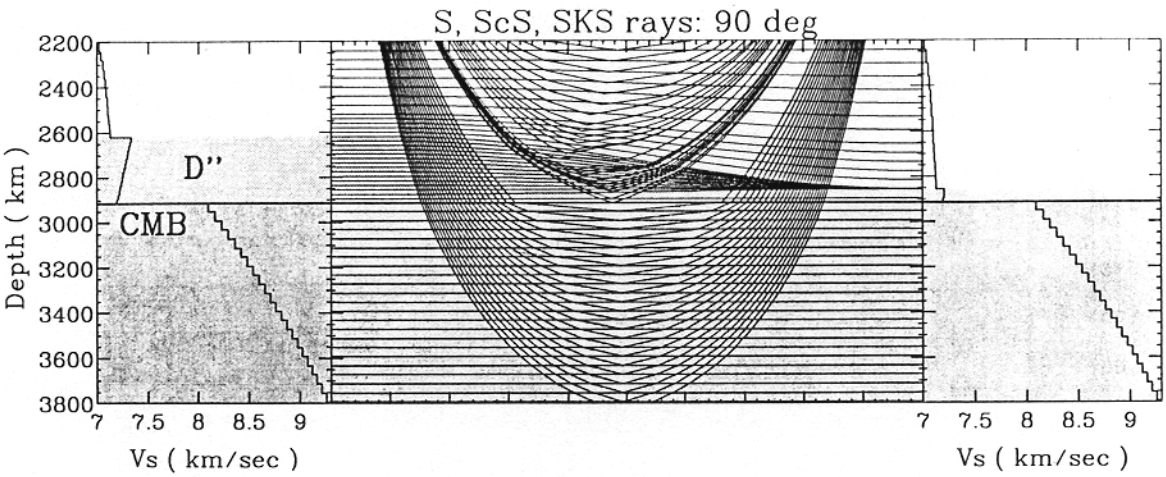

Figure 5.14 Display of a 2D earth flattened section starting with SYL1 on the left and ending with a possible mid-Pacific model proposed by Garnero *et al.* (1988). The middle panel displays some ray paths sampling the structure corresponding to position (c) at a range of 90°.

as well as to establish the type of observed features that prove difficult to treat with simple uniformly layered models. As in the previous section, we will again examine the observations of deep events; namely, one occurring beneath Java (Figure 5.15) and two beneath Fiji (Figure 5.16). Data from the former (Figure 5.17) appears to be well modeled by PREM with a few exceptions while examples of the latter (Figure 5.18) are poorly modeled by PREM.

In these comparisons, the traces are lined up on the SKS peak and maximum amplitudes are normalized to unity. The dotted lines indicate the arrivals of SKS, SPdKS, S2KS and S3KS. The phase SPdKS as introduced by Choy (1977) is generated by a *P*-diffraction occurring at both the SKS entrance and exit locations of the core-mantle boundary. Figure 5.19 displays these paths as dotted lines relative to the solid lines which are true geometric arrivals SKS and SKKS. Note that lateral variation in D″ is sampled nicely in both *P* and *S* by this family of arrivals. In Figure 5.17 the synthetics fit the data quite well, except at some stations such as YKC and PNT. These two paths indicate that SKKS-SKS is roughly 4 s larger in the data relative to PREM. Likewise, problems in the SKS and SPdKS waveform are particularly clear at these stations. These distortions are easily fixed by slowing down the *P*-velocity at the base of the mantle as discussed later. Thus a reduction in velocities at the base of the mantle can match observed anomalies in SPdKS-SKS and S2KS-SKS times, particularly when lateral variations are allowed.

The comparisons in Figure 5.18 are generally bad with a few stations that are not too far off, namely, GWC and SCH. Generally, the SKKS-SKS are separated too much in the data relative to PREM, and SPdKS develops much too fast in the data indicating a slow *P*-velocity at the base of the mantle, see Garnero *et al.* (1993c). Another difference exists in the SV diffracted phase where the data are much too large and late relative to PREM.

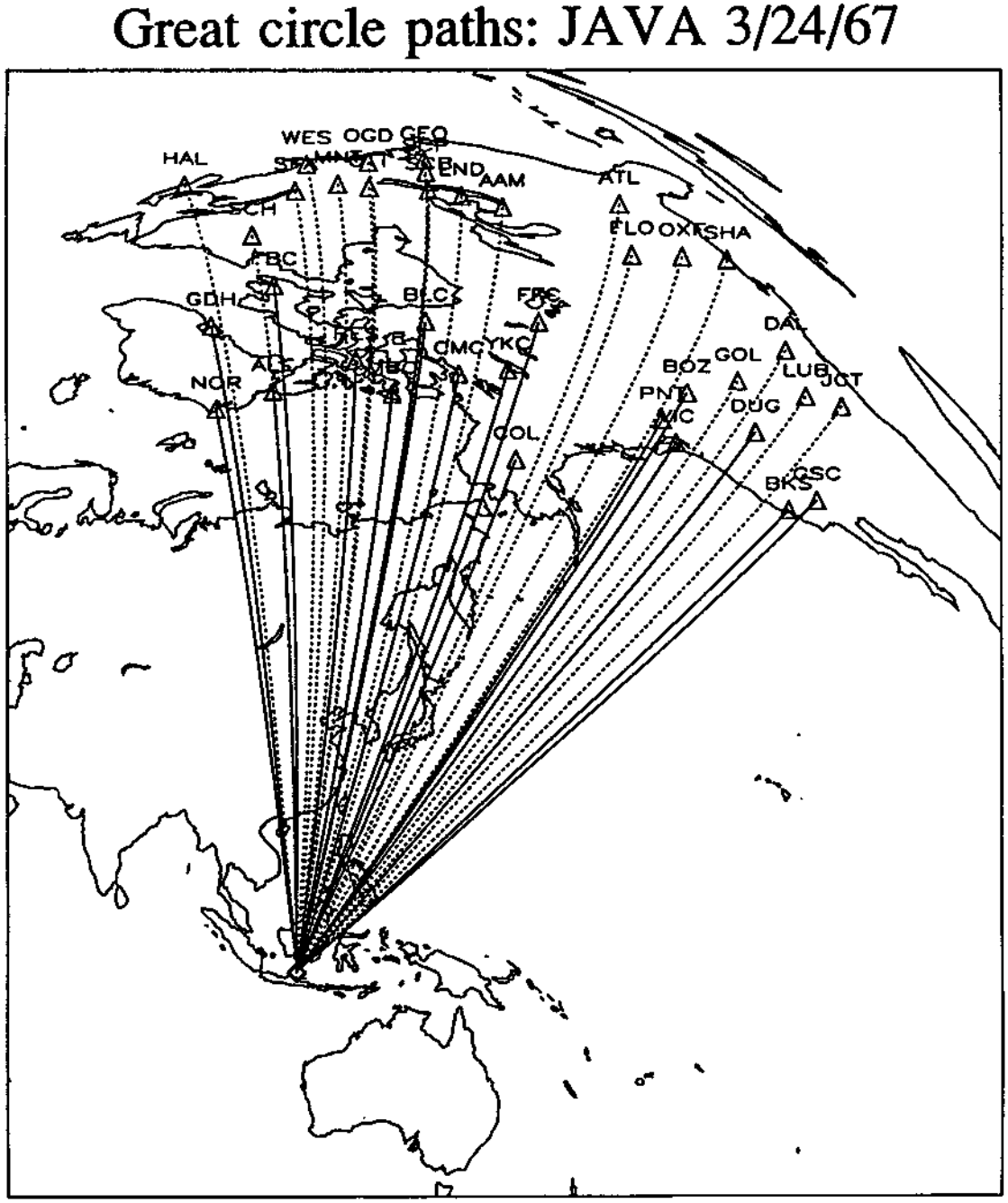

Figure 5.15 Map displaying paths from a deep Java event to WWSSN and Canadian stations (CSN). These paths are considered to be quite simple according to most tomographic models. Dotted lines are SmKS paths, and solid lines indicate SKS paths.

The data at larger ranges for these events are discussed in Garnero *et al.* (1993b) and Garnero and Helmberger (1995) where PREM works well for the Java event but poorly for the Fiji region.

If one compares the paths associated with the Java event with recent tomographic models, one sees that they sample mostly normal type structures, less than

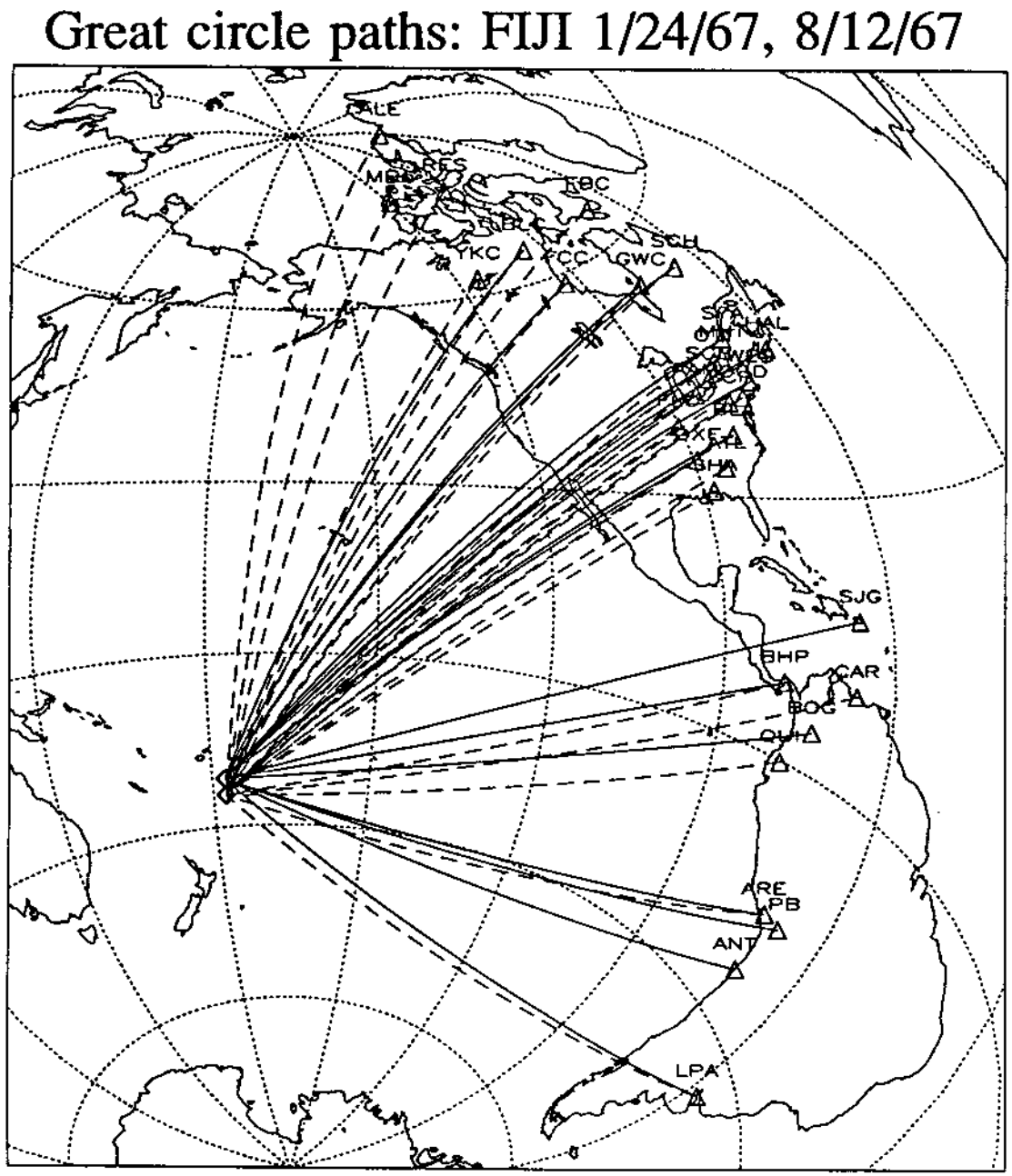

Figure 5.16 Map displaying paths connecting a deep Fiji event to the various analog stations. These paths are expected to be complex according to most tomographic models. Dotted paths are appropriate for event 8/12/67; solid lines for 1/24/69.

1% variation. In contrast, the paths sampled by the Fiji event encounter the strong Mid-Pacific anomaly, see Tanimoto (1990), Su and Dziewonski (1994), Masters *et al.* (1992) and others, with variation up to 4%.

In short, it appears that 2D and 3D structures at the base of the mantle are producing substantial waveform distortions in the data. If we can model these features, we can expect to further refine these structures, namely, their *P* and *S* veloc-

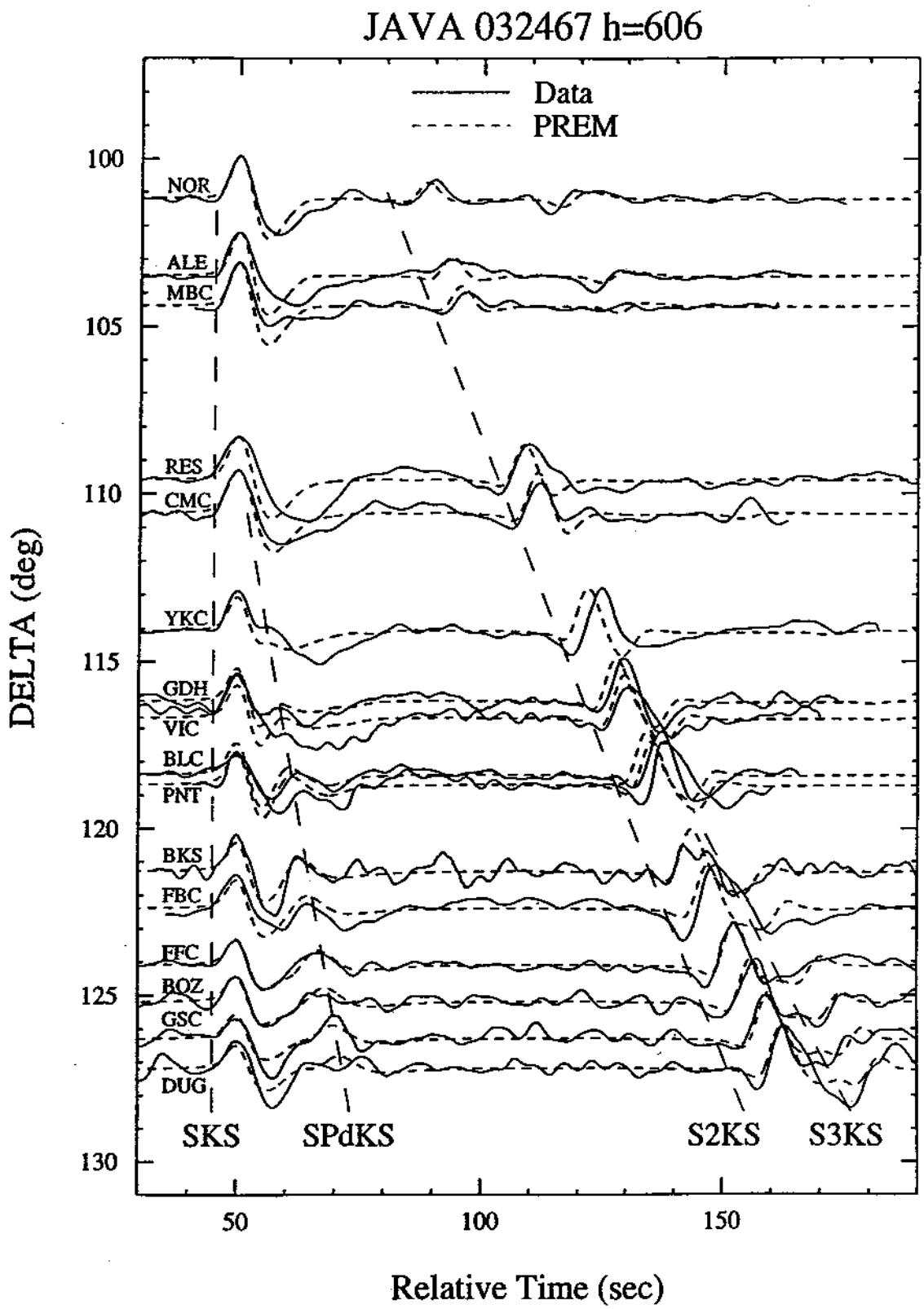

Figure 5.17 Comparison of observed and synthetic seismograms (LP, WWSSN) from the Java event. The synthetics were generated with a reflectivity code and are appropriate for the PREM model, after Garnero and Helmberger (1995).

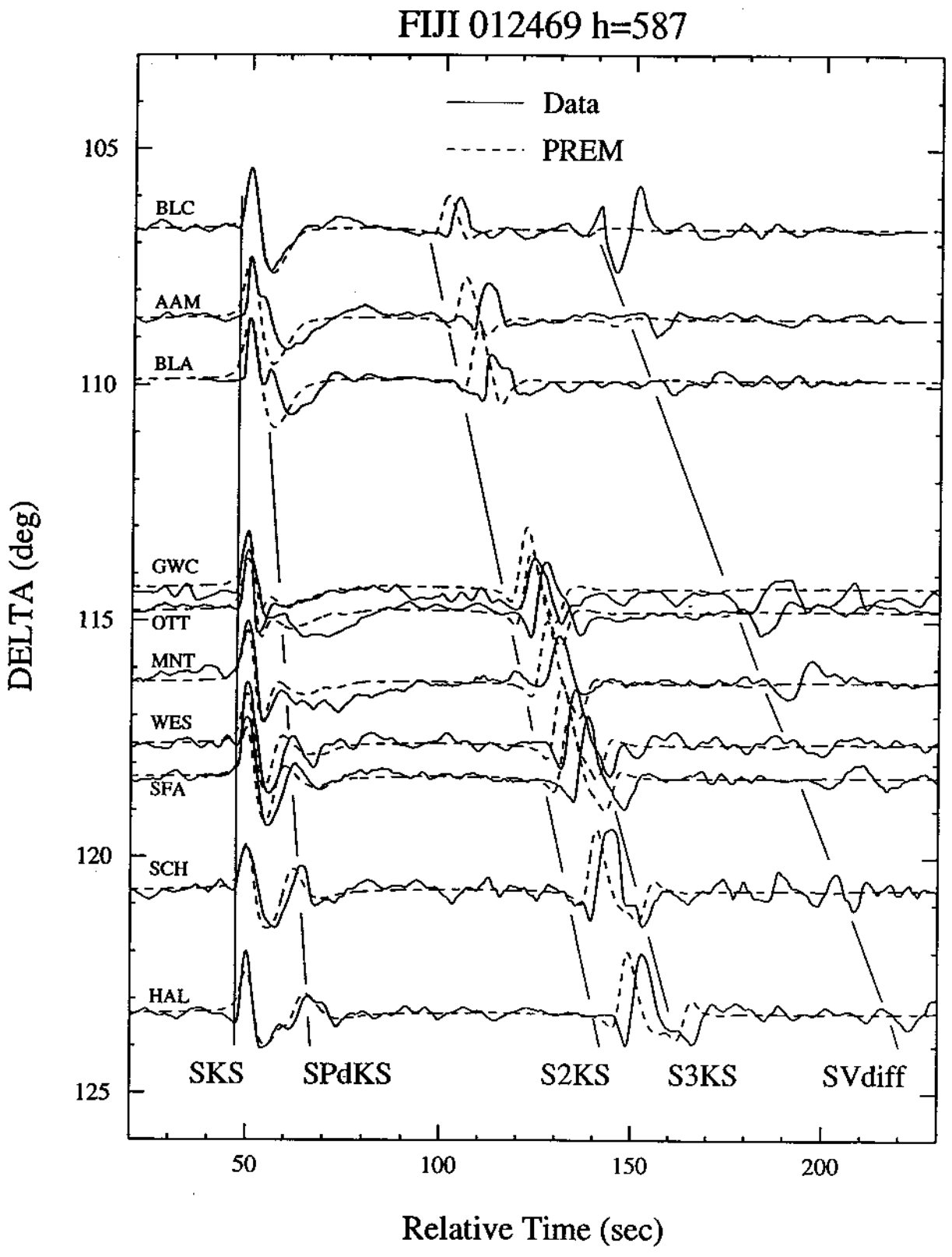

Figure 5.18 Comparison of observed and synthetic seismograms for one Fiji event. The synthetics were generated with a reflectivity code and are appropriate for the PREM model after Garnero and Helmberger (1995).

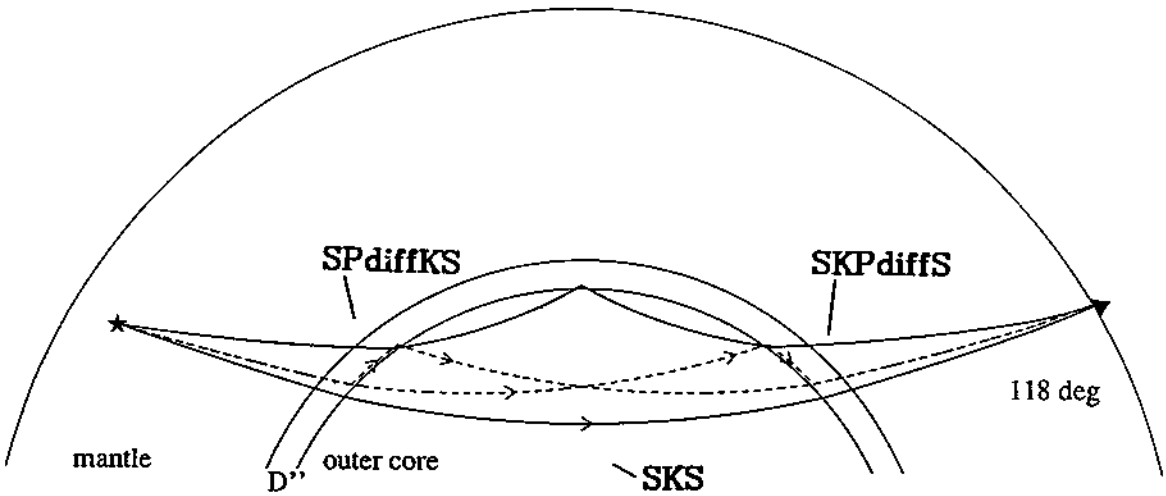

Figure 5.19 Display of ray paths associated with SKS, SKKS, SP_dKS and SKP_dS.

ity characteristics. The experience gained in comparing the above observations against synthetics suggest two types of numerical experiments. One involves the interferences of SKS and SPdKS at ranges 105° to 115° where they overlap. Because diffractions (SPdKS) are difficult to handle with WKB type codes, we will address this problem with Cagniard-de Hoop. The second experiment involves the timing issue associated with the SmKS phases and where one phase samples a particular 2D structure differently from another. It appears that WKM could be useful for this type of investigation. We will discuss this approach first.

5.4.1 *D″ heterogeneity and effects on SKS, SKKS ... (SmKS)*

Earlier in the lower mantle 2D structures, we considered a relatively smooth linear-type transition between two different D″ models. Here, we discuss the effects produced by a smooth but rapidly changing D″ with a cosine shaped low velocity depression (see Figure 5.20). It has a horizontal wave-length of 3000 km. The thickness of the zone of lateral variation depth of 500 km was assumed in this exercise. Included in Figure 5.20 are ray paths corresponding to S2KS and S3KS for a distance of 150°. Note that following the WKM approach, we must track rays from each of the iso-velocity interfaces in order to construct the $p(t)$ curve. The earliest arrival from each of these phase groups can be determined in the process of generating the synthetics. In Figure 5.21, we display 3 paths, the earliest and the two neighboring rays, for SKS (solid), SKKS (dotted), and S3KS (light) for four positions of the source relative to the anomalous structure. Record sections appropriate for these four source positions labeled 0, 1000, 2000, 3000 are displayed in Figure 5.22. We have included a 1D section on the left for comparison (essentially PREM). To understand these synthetics, we need to appreciate two factors, the geometric spreading features and the generalized transmission co-

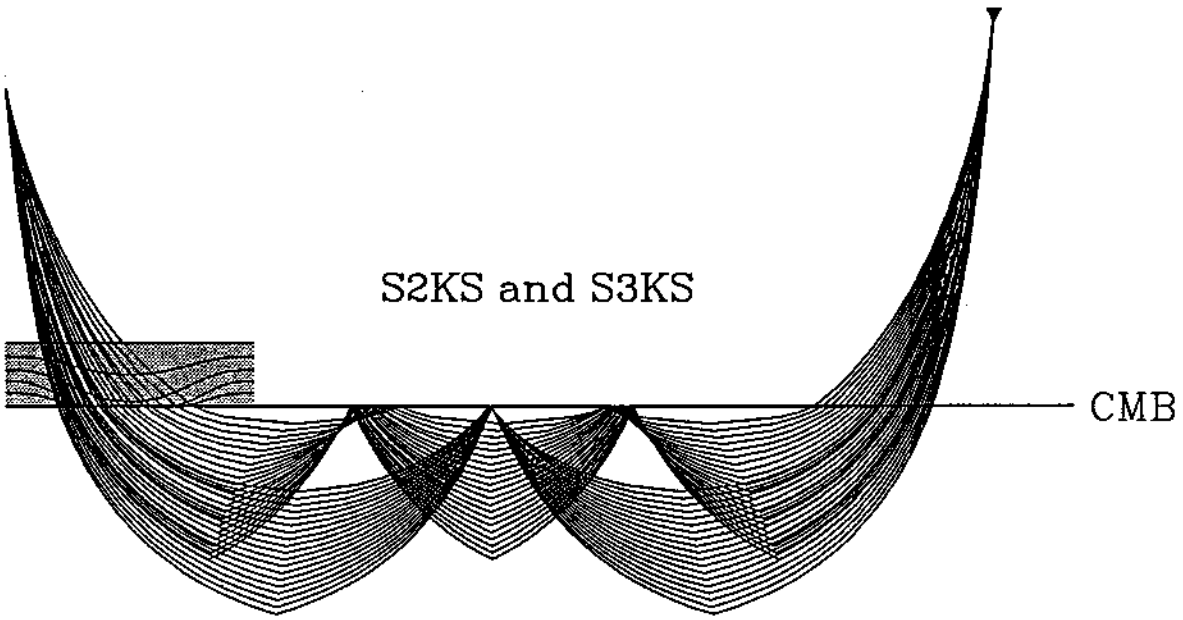

Figure 5.20 Display of ray paths connecting the various interfaces to the source and receiver for a 2D model.

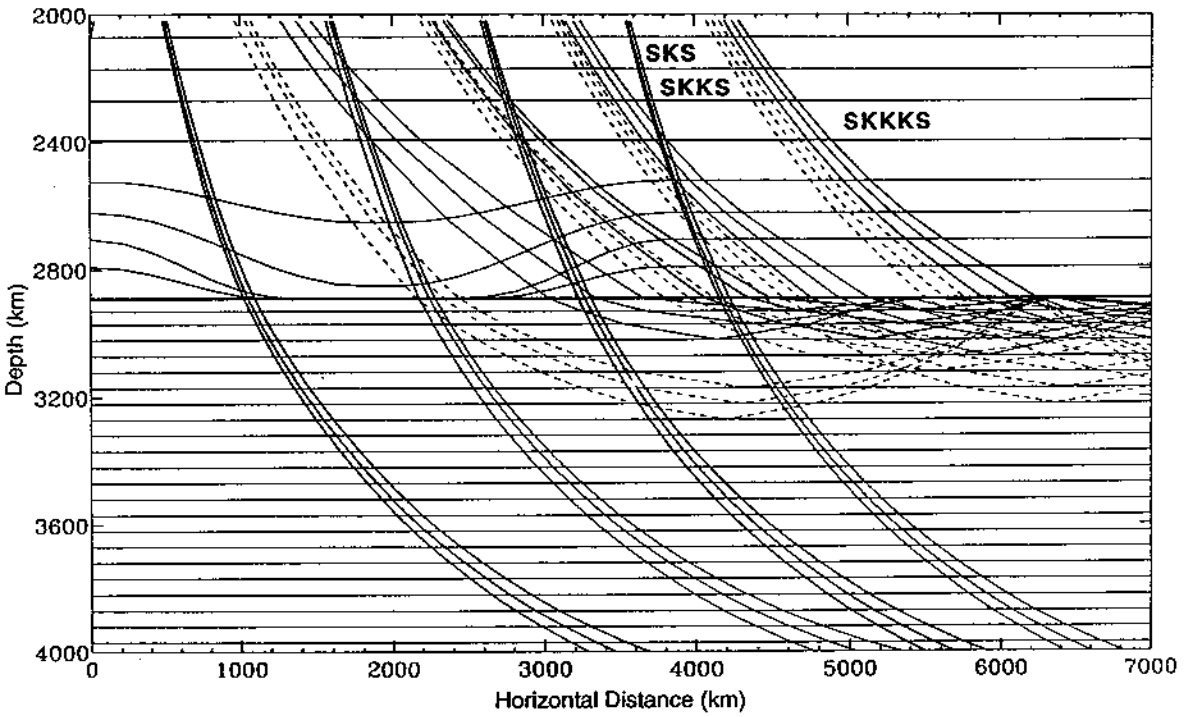

Figure 5.21 Display of a 2D velocity section showing iso-velocity lines serving as reflectors and some example ray paths for SKS (bold), SKKS (dotted), and S3KS (light).

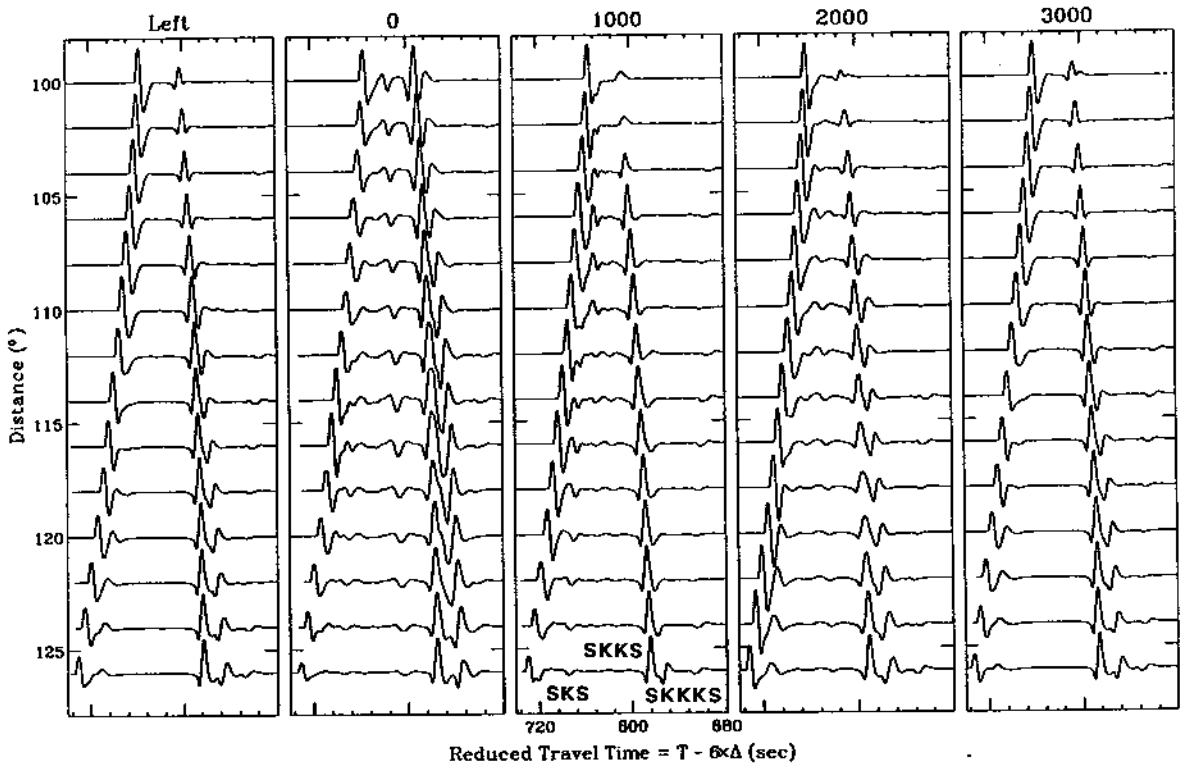

Figure 5.22 Synthetics corresponding to five source positions where the column on the left is essentially PREM and other four correspond to 2D seismic sections. These synthetics have a long period WWSSN instrument and a (1,1,1) trapezoid source function with the source at the surface.

efficient, $\Pi(p)$ or GC, introduced earlier. The latter function contains the transmission coefficients at the mantle-core boundary; namely, T_{sp} (S to P) and T_{ps} (P to S) when entering and leaving the core, see Helmberger (1968) for explicit expressions. A plot of their product, SKS, along with the expressions for SKKS, etc. are displayed in Figure 5.23 assuming the PREM model. The SmKS curves contain the appropriate number of reflection coefficients, Rpp, at the underside of the core-mantle boundary. We have, also, included symbols denoting the appropriate ray parameters for the various phases as a function of distance. This particular layered model is rather coarse, 50 km thick before earth flattening. Thus, the ray parameter sampling is also coarse, and the true minimum at $p_c \equiv$ (1./P-velocity at the CMB) was not obtained. A more detailed search for p_c (thinner layers) does, indeed, finds GC = 0 for SKS, near 107°. At this range, SKKS is relatively large as indicated in the figure, and the ratio of (SKKS/SKS) on short period instrument becomes observationally large as discussed recently by Silver and Bina (1993).

We can gain considerable insight into this interesting phenomena by examining the combination of Figure 5.23 and the (t versus p) plots used in the generation of WKM synthetics. However, the amplitude of WKM synthetics are controlled by the product of GC and ($\delta p/\delta t$) computed as a function of (t). At the minimum time the ($\delta p/\delta t$) curve has a well-known square-root singularity, Chap-

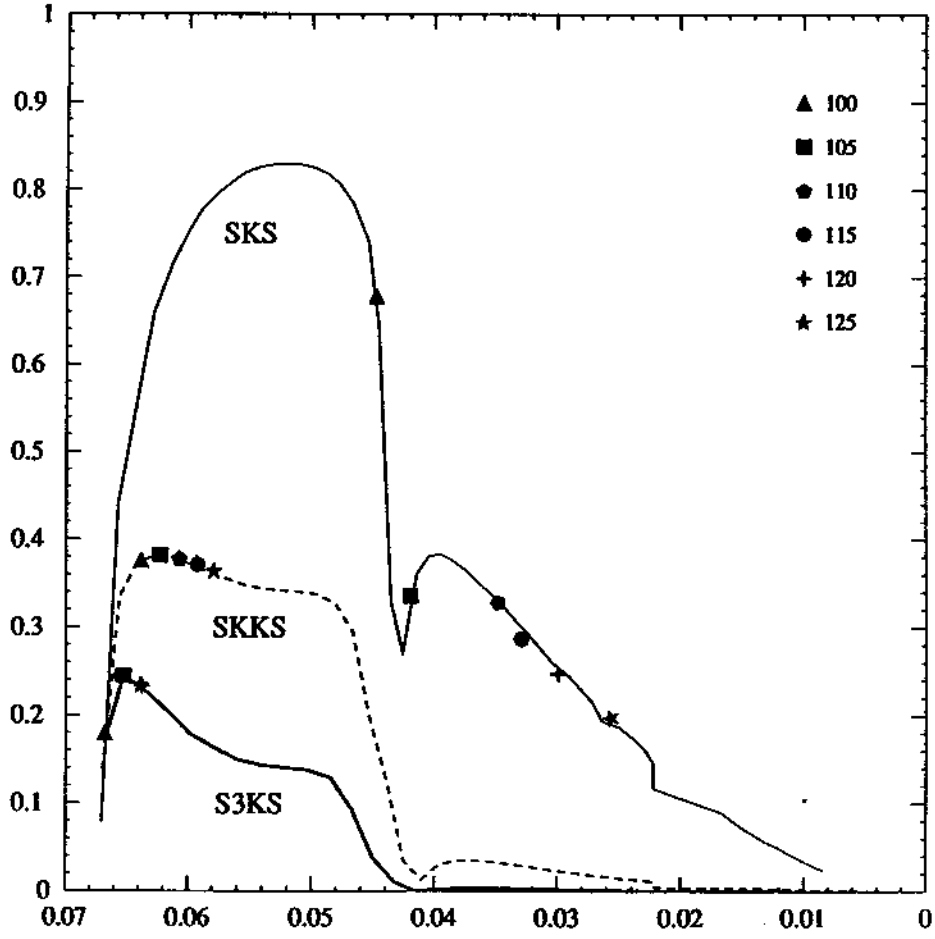

Figure 5.23 Plot of amplitude (GC) versus ray parameter in earth flattened coordinates showing the rapid variation of SKS near (p = .04) or $p = 1/\alpha$ (the P-velocity at the base of the mantle). Symbols indicate the ray parameter appropriate for the various distances and phases.

man (1976), and yields the geometrical solution at the limit of infinite frequency. However, if GC happens to be zero at this point, (p_c), the product is zero and SKS is zero. But because the GC curve increases rapidly away from p_c, small changes in p lead to large increases in GC and the SKS amplitude becomes strongly a function of period. Note that it also becomes a strong function of the details of the model, both in parameterization and structure of D″ as can be seen in the 2D record sections. The amplitudes in Figure 5.22 are scaled relative to the top trace of the column on the left, that is, the homogeneous case ($\Delta = 100°$) with all other ranges and cases relative to this value. Thus, the weakest SKS signal occurs for case (0) at $\Delta = 126°$ and the strongest at case (1000) for $\Delta = 100°$. Most of the dominant features displayed in this figure are controlled by geometric spreading with late arrivals generally strong and early arrivals generally weak relative to the homogeneous case. The most noticeable example is the SKKS arrival at $\Delta = 100°$ (case 0) where this phase is about 4 to 6 s slower than PREM in absolute time.

To emphasize the geometrical nature of these effects we have plotted the ray paths of the earliest ray and the rays bottoming at adjacent layers in Figure 5.21. The relative "δp" and "δt" between these rays in conjunction with GC control the initial motions, see Hong and Helmberger (1978). For example, the SKKS set of rays that cross the slowest portion of the anomaly bottom deeper in the core than in the other cases. This leads to stronger motions because of the enhanced GC. In contrast, the SKS is faster since it does not sample the anomaly quite so strongly.

When interesting arrivals such as the pulse midway between SKS and SKKS occur, we can also plot-out the full (p,t) curve and determine its origin. In this case, it is caused by the pinching-out of layering occurring on the SKS path as it crosses the CMB (see the rays on the far left in Figure 5.21.) Thus the modeler can interrogate various features and worry about model artifacts. In short, the WKM method is quite useful in exploring 2D models because we can easily detect the significance of any particular pulse and thereby interpret observation in a meaningful fashion. However, there is some concern about the proper handling of the SP_dKS phase in the 105° to 112° range which we will address in the next section.

Nevertheless, it appears that WKM can be very useful in explaining the relative timing and amplitude ratios of multi-bounce SKS phases at ranges beyond 115° as demonstrated in Figure 5.24. The first two columns, (a) and (b), display 1D

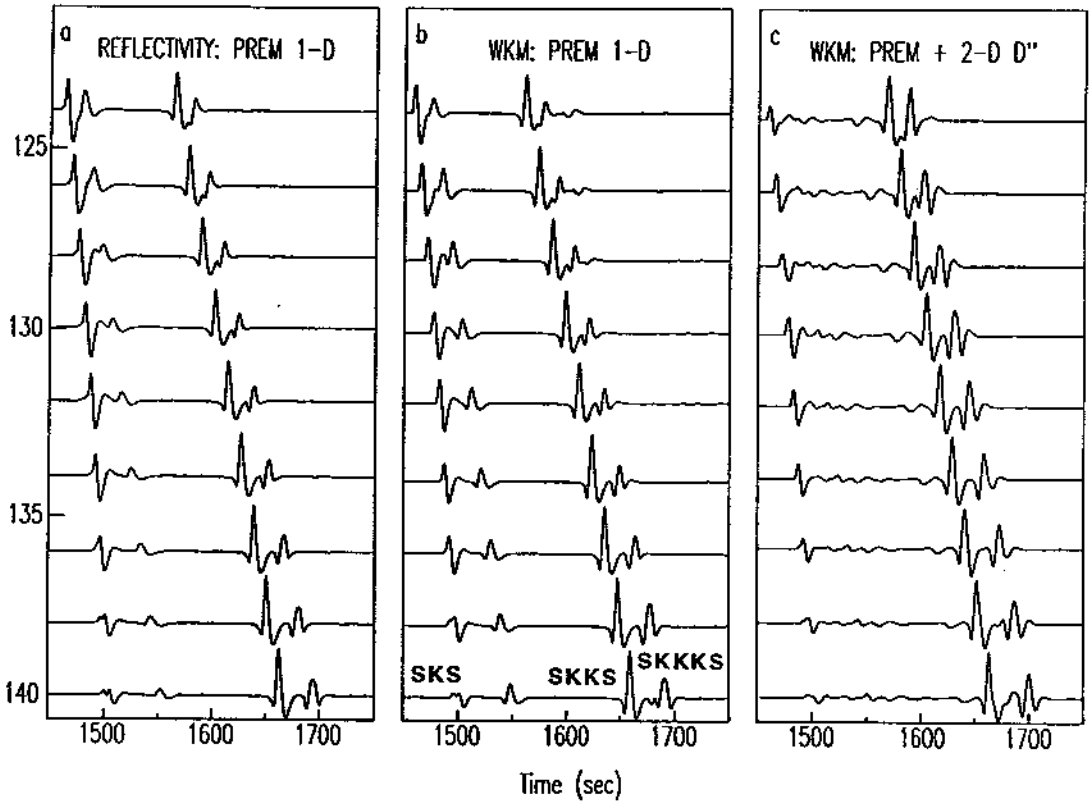

Figure 5.24 Comparison of reflectivity and WKM synthetics for the PREM model along with synthetics for the 2D model.

responses passed through a LP WWSSN instrument, and reaffirm the adequacy of the WKM technique in the simulation of these responses. The third column, (c), displays synthetics appropriate for position (o) discussed earlier. A comparison of (b) and (c) indicates that SKKS in (c) is shifted back by up to 6 s relative to SKS at some ranges where it samples the middle of the slow anomaly. The 2D structure changes the SKKS ray paths, causing them to dive more deeply in the core, resulting in a further delayed arrival time. Secondly, the concave nature of the structure also enhances its amplitude. That is, late arrivals usually arrive stronger which is a well-known geometrical feature.

The strengths of the multi-bounce SKS such as S3KS is quite apparent at the larger distances, as is S4KS at still larger distances. These multiples are, also, quite obvious in WWSSN record sections and can be used to constrain the structure of the outermost core velocity, Garnero *et al.* (1993b). Moreover, there are regions where these multiples show considerable lateral variation as reported by Garnero (1994). We plan to model these records with this code which appears ideal for this purpose.

5.4.2 *Modeling SP_dKS*

We know that the phase SP_dKS is associated with a *P*-wave that travels along the base of the mantle for a portion of its path. Since the phase velocity of rays bottoming near the depth of 3900 km in the core approaches that of the *P*-velocity at the base of the mantle (α = 13.7 km/s), rays can become critical and develop headwaves, see the upper panel of Figure 5.25. As the figure shows, the diffraction occurs equally on both the source and receiver sides of the path for 1D structures. To break this symmetry, we will assume that the *P*-velocity is reduced by 5% for one side of the path (α_s) but the other side has a "normal" CMB velocity (α_f), and construct synthetics in terms of ray summations as displayed in Figure 5.26. The bottom trace is the contribution of a ray bottoming at a depth of 3800 km, layer number 240 in the model used. The corresponding Cagniard-de Hoop complex *p*-plane is displayed in the lower portion of Figure 5.25. Two branch cuts are associated with the two mantle *P*-velocities, α_f and α_s. The Cagniard contour runs along the real axis until it reaches p_0 and becomes complex. Since the transmission coefficient, GC, becomes complex when encountering the branch cuts we expect head waves as indicated. These head-wave contributions can be seen in the step response labeled $t(\alpha_f)$ and $t(\alpha_s)$ in Figure 5.26. Since GC is complex, there will be a strong contribution to the response both before and after $t(p_0)$. The precursor portion of the response is sometimes referred to as the tail-of-the head wave response. The closer $t(p_0)$ is to the tip of the branch cut, $p_c = 1/\alpha_s$, the stronger this response. Thus, the contributions of the five deeper layers, 240-245, creates a strong phase associated with α_s (Figure 5.26). Note that this energy is coming from a rather narrow range of depths, roughly 50 km, since the layer thicknesses are set at 10 km. A similar feature is produced when the contour crosses the $p_c = (1/\alpha_f)$, branch cut.

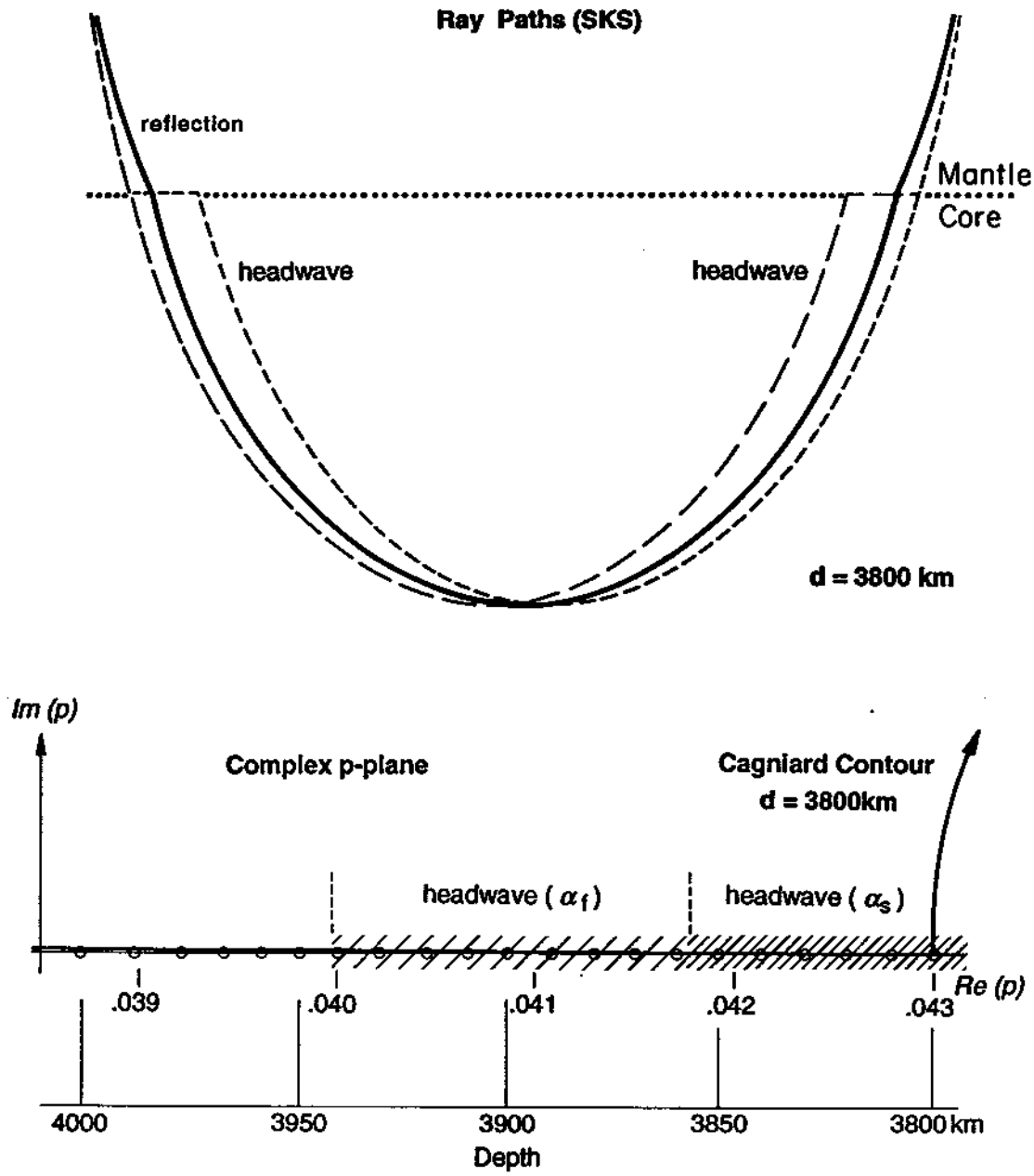

Figure 5.25 Upper panel displays the paths appropriate for SP_dKS and SKP_dS in PREM. These paths lose their symmetry for laterally varying models when the branch-cuts become distinct as displayed in the lower panel. The Cagniard contour displayed is associated with a ray bottoming at a depth of 3800 km (layer 240). The small circles indicate the p_0's associated with the other generalized rays contributing to the 2 diffracted pulses.

When $\alpha_f = \alpha_s$ in the 1D case, these two branch cuts come together and produce a single pulse. Figure 5.27 displays the GRT ray summation in this case for PREM. The rays are summed in three groups in this figure where the response that starts the latest, the upper trace of each group, includes rays down to layer 228 (depth of 3600). The next set includes rays down to 254 (depth of 3950) and

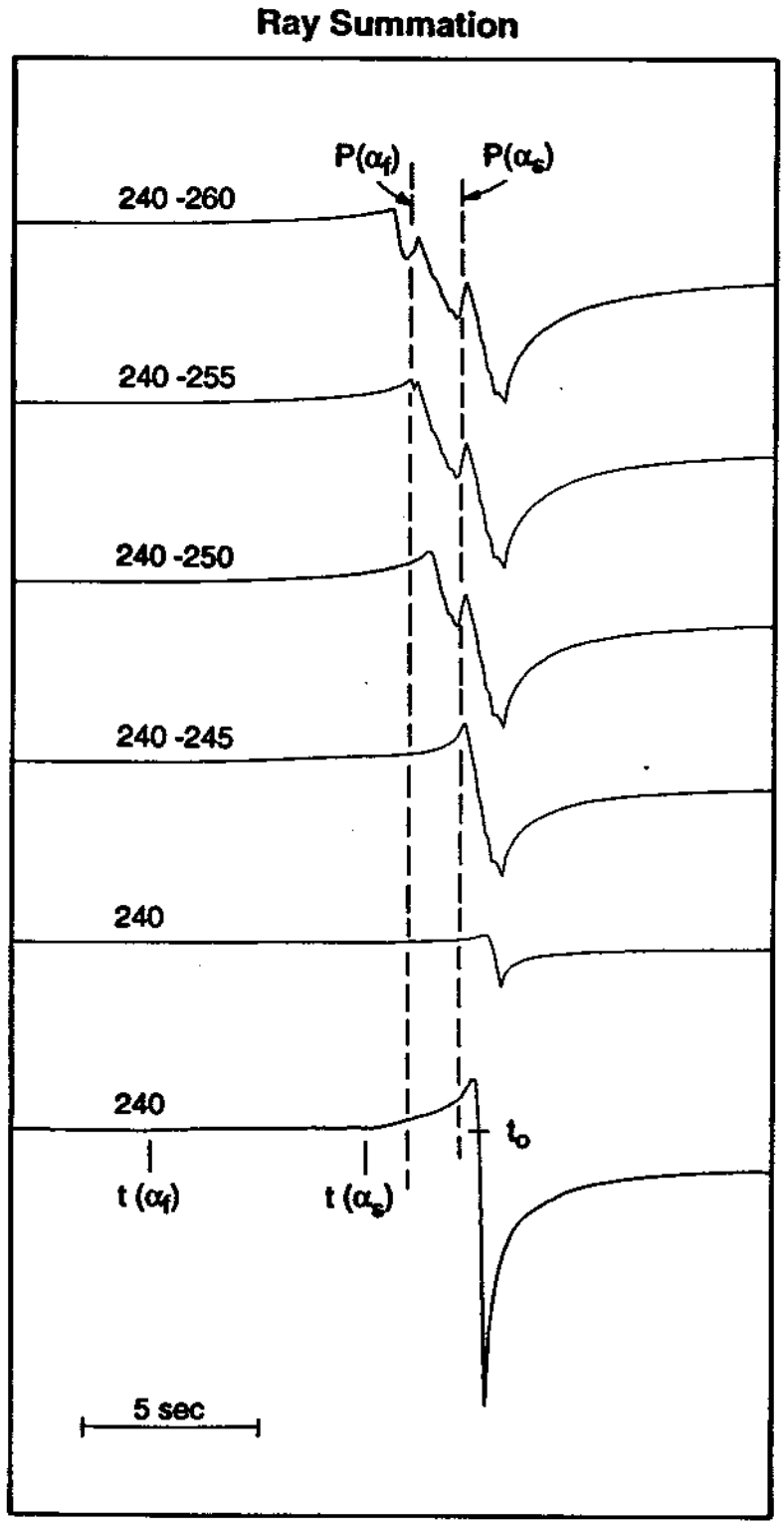

Figure 5.26 This figure shows the construction of P_{diff} from the summation of generalized rays. The bottom trace is the step response appropriate for the contour displayed in Figure 5.19 indicating the two headwaves starting at $t\alpha_f$ and $t\alpha_s$. The remaining traces are on the same amplitude scale and indicate the summation process as we add five rays at a time moving up the stack of layers.

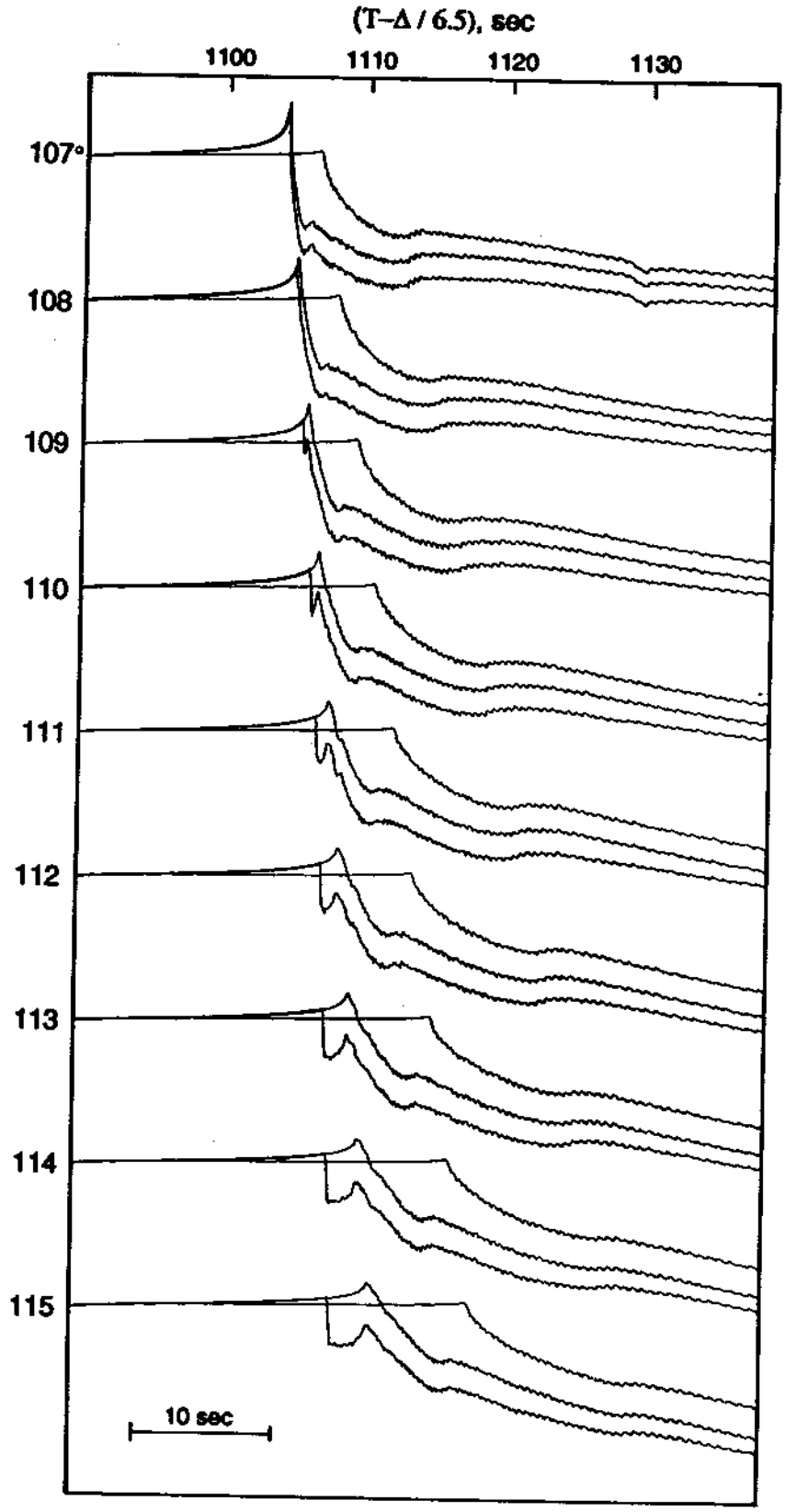

Figure 5.27 The figure shows the ray-summation process as a function of range for PREM.

the complete set including rays down to the inner core is given on the bottom trace of each group. Thus, the upper 800 km of the core does not contribute much to the responses at these ranges. The next few hundred km (800-1100 km below the CMB) controls the diffracted *P*-portion of the response. Since the geometric turning ray appropriate for a range of 107° bottoms at this depth, the entire response is controlled by these relatively few rays. That is, the entire response is dominated by P_{diff} as pointed out by Choy (1977). At greater ranges, the SKS pulse (a step in shape) emerges at 109° and moves out in distance. The delta function response and the synthetics appropriate for a short-period event are given in Figure 5.28. These results (PREM) are very similar to the reflectivity synthetics presented in Garnero *et al.* (1993c) as expected. The corresponding responses for

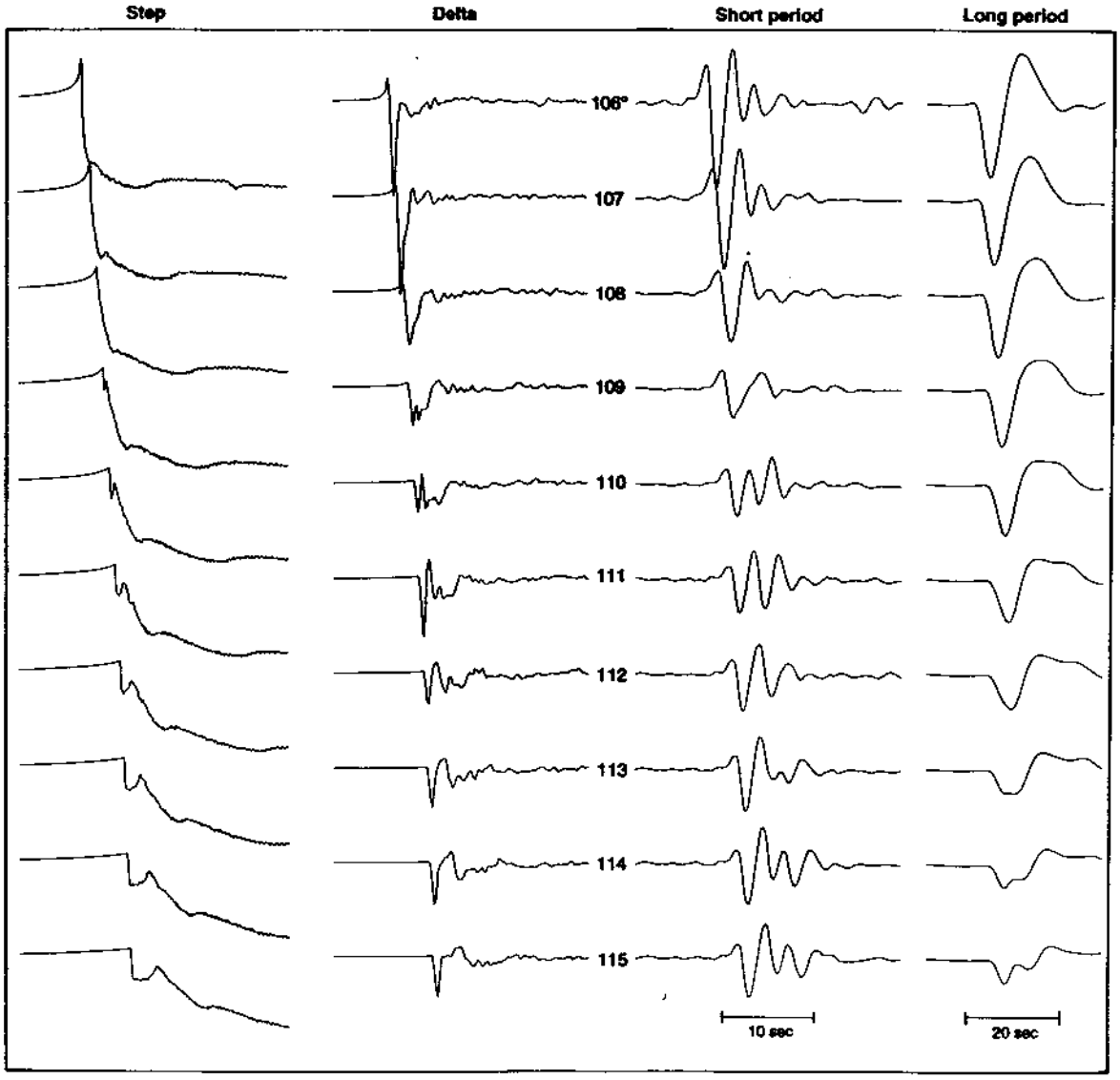

Figure 5.28 This figure displays the complete SKS PREM response as a function of range in terms of step, delta, short period synthetic, and long period synthetic.

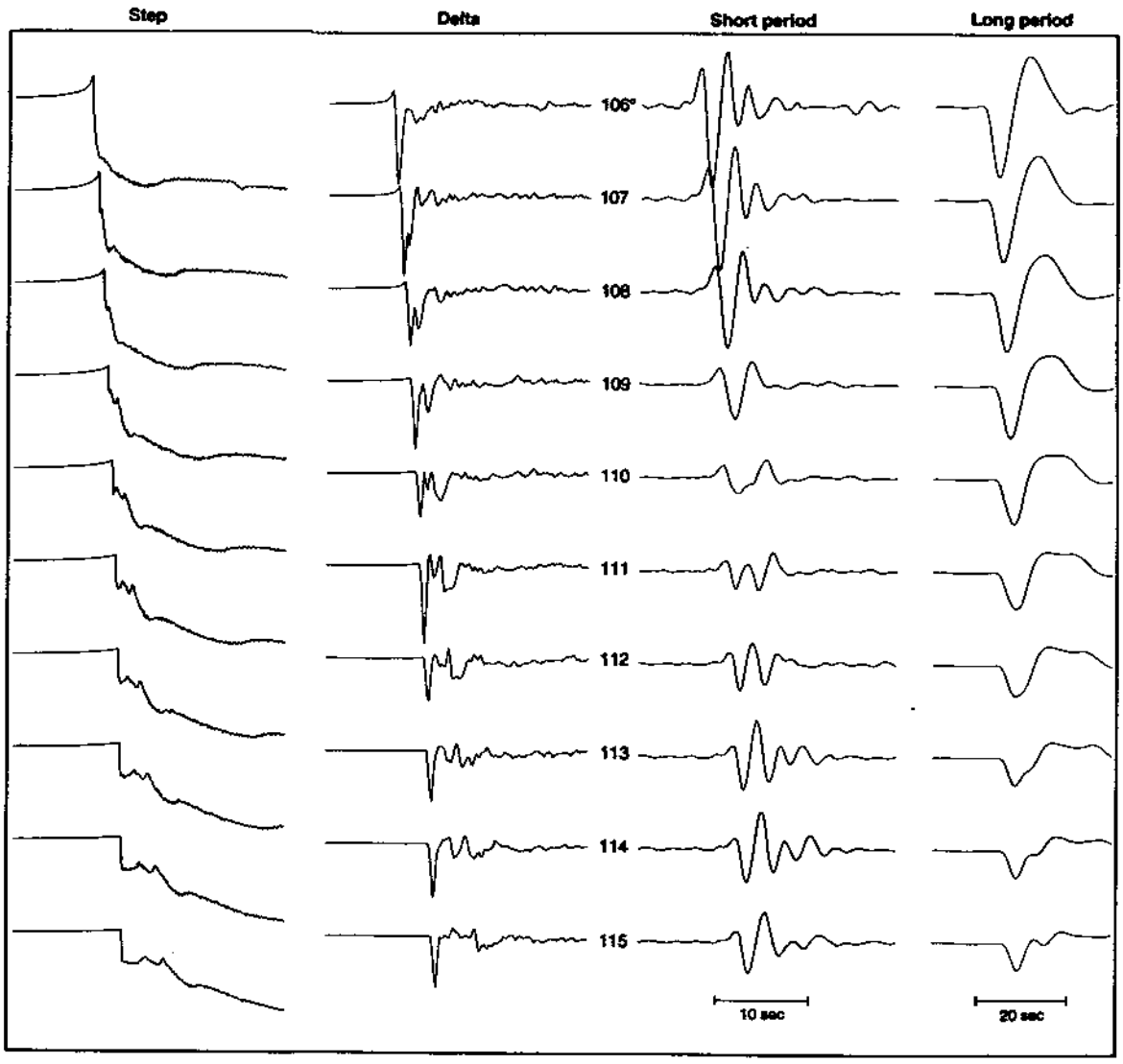

Figure 5.29 Complete SKS responses for a PREM-like model except the *P*-velocity is reduced by 5% along one of the mantle paths.

the non-symmetric model is displayed in Figure 5.29. The periodicity of the assumed source and instrumental response interacts with the SKS-SP_dKS separation to produce a rather complicated wavetrain. But the overall reduction in short-period amplitudes of the synthetics of up to a factor of 4, as observed by Silver and Bina (1993), is easily obtained. However, the position of this minimum and waveform distortions is quite event-dependent and will require special attention. Also included in Figures 5.28 and 5.29 are the long-period synthetics assuming a $t^* = 3$, a trapezoid source history, (1,1,1), and a WWSSN instrument. As expected, the reduction in long period SKS amplitudes is more subdued.

Some results of modeling using this approach are given in Figure 5.30. The observations are from a Fiji event (12 Aug. 1967, $M_6 = 6.5$, depth = 134 km). The

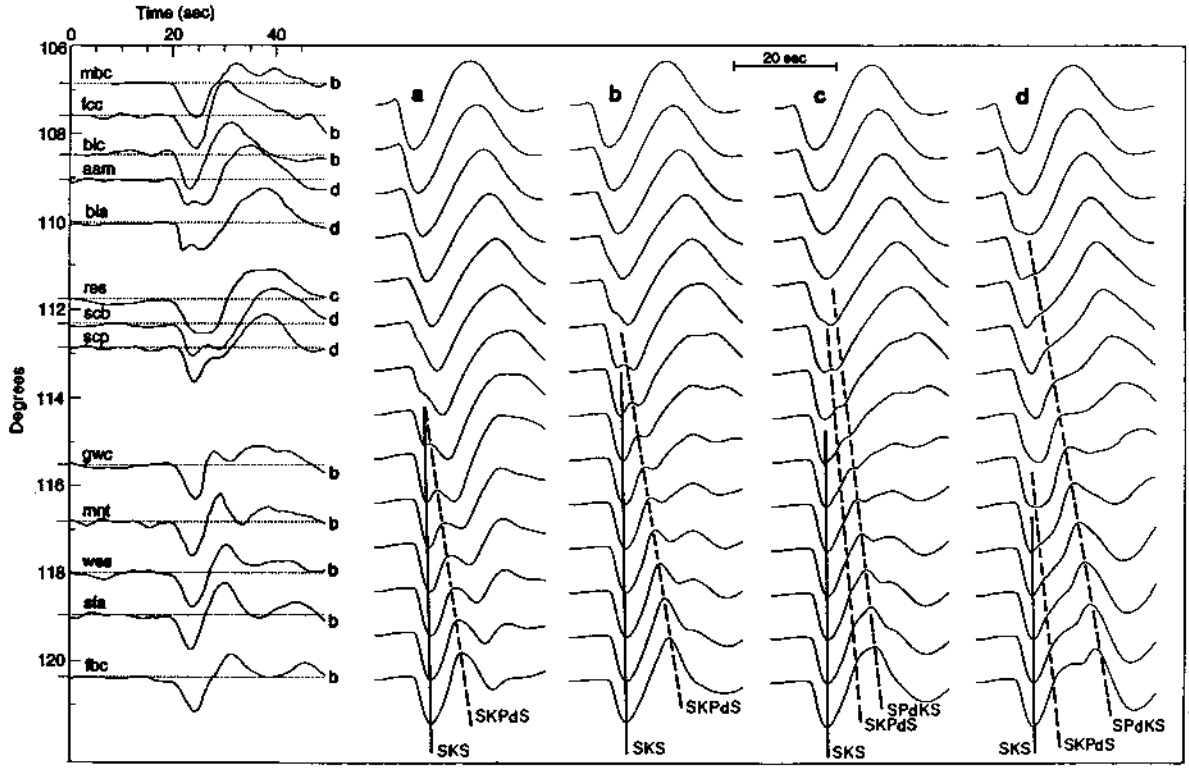

Figure 5.30 Comparison of a profile of observations from a Fiji event with possible models. Solid lines indicate the SKS phase and dotted lines indicate the SP_dKS and SKP_dS phases.

paths from this event were included in the earlier Figure 5.16 which are similar to those of the other Fiji event. Since this is a rather large shallow event, we have not included the SKKS phases which are contaminated by surface reflections. But the complexity of the SKS phases at particular stations is quite similar to those in Figure 5.18. That is, stations AAM and BLA show the same distortions relative to the simple pulse at BLC. The stations SCP and SCB in Figure 5.30 are along the same path as AAM and they show similar complexity. Obviously, PREM does a poor job of predicting these complexities as demonstrated in Figure 5.18, except for BLC. Garnero *et al.* (1993c), using synthetics generated with reflectivity, demonstrated that many of these complexities could be modeled by dropping the *P*-velocity at the base of the mantle. We have included this model in our Figure 5.30 as case (b). Case (a) is PREM; (c) contains a -8% (source region) and a -3% (receiver region) and (d) contains -9% (source region) and a $+3\%$ at the receiver region. We have added some dashed lines to roughly indicate the onsets of the diffractions. Comparing these synthetics with the observations is complicated in that the latter contain a mixture of instruments with each Canadian station having a particular response. Stations AAM, BLA, SCP and WES are part of the WWSSN system while the others are from the Canadian network which are slightly shorter period in general. Nevertheless, if we overlay these synthetics with these records, we conclude that (d) does a reasonable job of modeling AAM

BLA, SCB and SCP, while (b) and (c), which yield similar synthetics, explain the others at the more northly azimuths.

The synthetics presented here are quite idealized especially at the larger ranges. That is, we are assuming that the transmission coefficient is independent of the basal mantle layer thickness which is not the case if the layer is thin, see Garnero *et al.* (1993c). The effect shows a range dependence and a frequency dependence as one might expect from a diffracted phenomenon. Thus, the simple types of GC behavior assumed here, see Figure 5.31, would change to become more PREM-like at larger ranges. It would appear that more observations are needed to fix the scale lengths of these anomalous structures as well as more 2D and 3D modeling work to appreciate these waveforms.

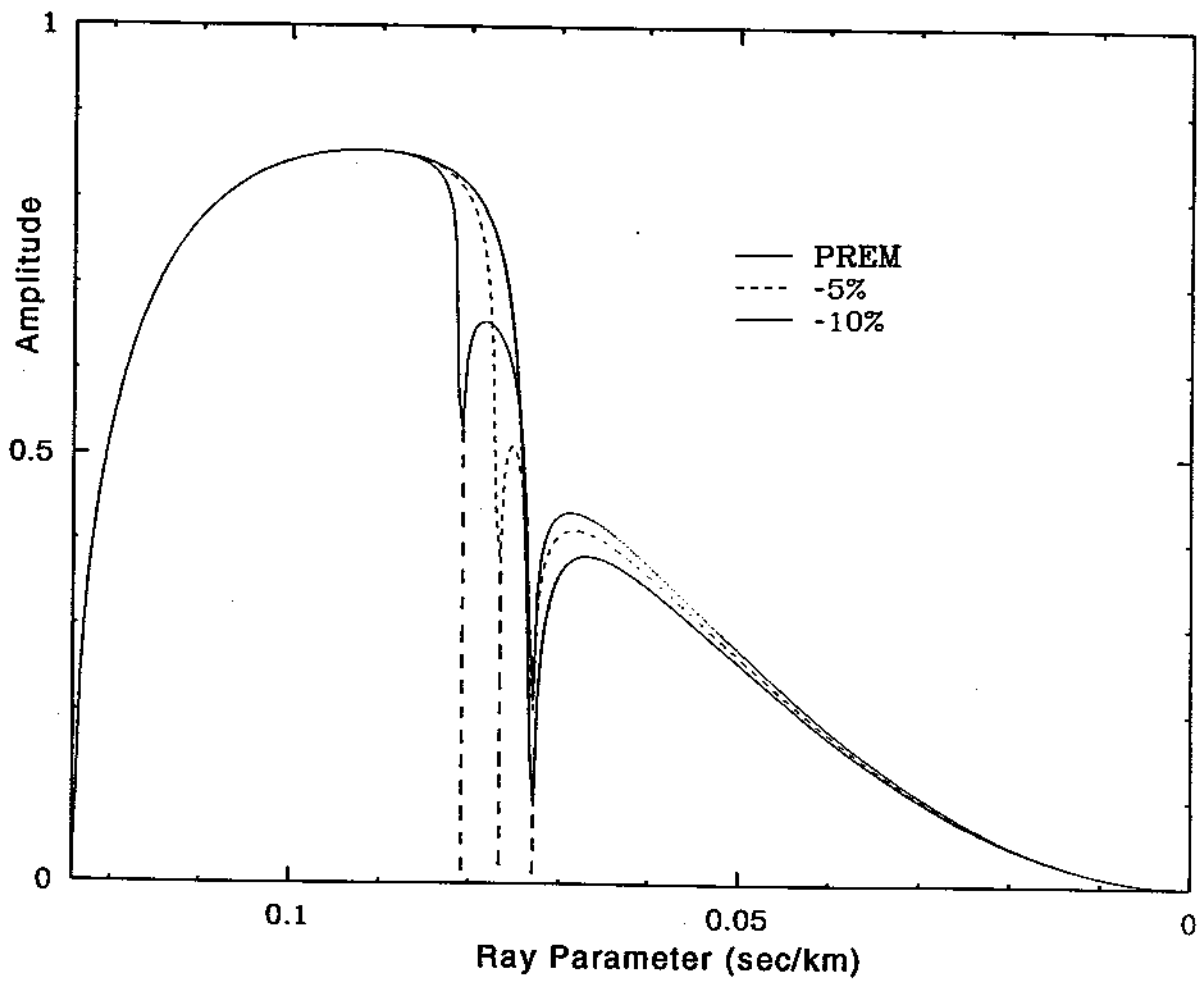

Figure 5.31 Plot of GC amplitudes as a function of ray parameter (s/km) for three models. The solid heavy line is appropriate for PREM. The dashed line is for the case of a 5% reduction in velocity at one end, and the light line for the case of a 10% reduction. Heavy dashed lines have been added to show the true zeros at the three *P*-velocities. These values are plotted with respect to a spherical earth so that they are the true velocities before the earth flattening approximation has been applied.

5.5 Discussion and conclusions

In the above applications, we discussed an example of 2D ray tracing and Cagniard-de Hoop synthetics at cross-over distances for SKS and *S*. These synthetics are reasonably accurate except at the larger ranges where core-diffraction is occurring and multiples become important. Ray theory limitations have been discussed previously, see Lay and Helmberger (1983), and are surely exaggerated by the 2D structure. Nevertheless, we think these synthetics will be quite useful in interpreting observations in the usual applications of synthetics. When a clear image of a detailed structure emerges from such attempts, we suggest that the above type of synthetics be checked against other analytical techniques or, perhaps, more exact methods such as the hybrid numerical-analytical interfacing techniques, see for example Stead and Helmberger (1988), and others. We did not attempt to use the ray path mapping from the WKM code to generate Cagniard-de Hoop synthetics at present but this will be pursued in future efforts. Still another interesting strategy to explore in waveform modeling is in terms of pseudo 1D models where the layer thicknesses and velocities, such as in D″, are allowed to vary as a function of position.

The extra degrees of freedom would be very useful in producing better fits and recovering the true 2D model could be attempted by performing the inverse mapping as a second stage. That is, we would forward model D″ in the prime system (see eq. (5.6)) and transform back into the real 2D or 3D structure when sufficient fits become available.

In summary, this paper presents some useful techniques for generating synthetics for 2D structures. We suggest a multi-stage approach where a modified WKBJ method is used to determine the importance of ray parameter distortions caused by the structure. Example calculations demonstrate the importance of these ray distortions that are neglected in tomographic investigations.

This new version of WKBJ is called WKM and tracks rays from interfaces embedded in the structure to construct the $(\delta p/\delta t)$ curve as opposed to the usual ray shooting techniques. All rays arrive at the receiver using WKM and correspond to the same p_0's and t_0's associated with the Cagniard-de Hoop technique. These ray tracks can be used directly in a 2D Cagniard-de Hoop code or they can be used to map the 2D structure into a local 1D structure, called the local stretching approximation.

Acknowledgements

We would like to thank Xiaoming Ding for his help in generating a number of these figures. This research was supported by the National Science Foundation, grant EAR93-16441, and by the Air Force Office of Scientific Research under grant F49620-92-10221. Contribution 5340, Division of Geological and Planetary Sciences, California Institute of Technology, Pasadena, California, 91125.

REFERENCES

BURDICK, L.J. and C.A. SALVADO (1986): Modeling body wave amplitude fluctuations using the three dimensional slowness method, *J. Geophys. Res.*, **91**, 12482-12496.

CHAPMAN, C.H. (1974): Generalized ray theory for an inhomogeneous medium, *Geophys. J. R. Astron. Soc.*, **36**, 673-704.

CHAPMAN, C.H. (1976): Exact and approximate generalized ray theory in vertically inhomogeneous Media, *Geophys. J. R. Astron. Soc.*, **46**, 201-233.

CHAPMAN, C.H. and R. DRUMMOND (1982): Body wave seismograms in inhomogeneous media, *Bull. Seism. Soc. Am.*, **72**, s277-s318.

CHAPMAN, C.H. and J.A. ORCUTT (1985): The Computation of body wave synthetic seismograms in laterally homogeneous media, *Rev. Geophys.*, **23**, 105-163.

CHOY, G.L. (1977): Theoretical seismograms of core phases calculated by frequency-dependent full wave theory, and their interpretation, *Geophys. J. R. Astron. Soc.*, **51**, 275-312.

CHOY, G.L., V.F. CORMIER, R. KIND, G. MÜLLER and P.G. RICHARDS (1980): A comparison of synthetic seismograms of core phases generated by the full wave theory and by the reflectivity method, *Geophys. J. R. Astron. Soc.*, **61**, 21-39.

DING, X. and D.V. HELMBERGER (1995): Modeling the D″ structure beneath Central America with broadband data, *Geophys. J.R. Astron. Soc.* (submitted).

DZIEWONSKI, A.M. and D.L. ANDERSON (1981): Preliminary reference earth model (PREM), *Phys. Earth Planet. Inter.*, **25**, 297-356.

FRAZER, L.N. and R.A. PHINNEY (1980): Computation of body wave synthetic seismograms in inhomogeneous media, *Geophys. J. R. Astron. Soc.*, **63**, 691-717.

GARNERO, E.J. and D.V. HELMBERGER (1993): Travel times of *S* and SKS: Implications for 3D lower mantle structure, *J. Geophys. Res.*, **98**, 8225-8241.

GARNERO, E.J. and D.V. HELMBERGER (1995): A very slow basal layer underlying large-scale low velocity anomalies in the lower mantle beneath the Pacific: evidence from core phases, *Phys. Earth Planet. Inter.*, **91**, 161-176.

GARNERO, E.J., D. HELMBERGER and G. ENGEN (1988): Lateral variations near the core-mantle boundary, *Geophys. Res. Lett.*, **15**, 609-612.

GARNERO, E.J., D.V. HELMBERGER and S.P. GRAND (1993a): Preliminary evidence for a lower mantle shear wave velocity discontinuity beneath the Central Pacific, *Phys. Earth Planet. Inter.*, **79**, 335-347.

GARNERO, E.J., D.V. HELMBERGER and S.P. GRAND (1993b): Constraining outermost core velocity with SmKS waves, *Geophys. Res. Lett.*, **20**, 2463-2466.

GARNERO, E.J., S.P. GRAND and D.V. HELMBERGER (1993c): Low *P*-velocity at the base of the mantle, *Geophys. Res. Lett.*, **20**, 1843-1846.

GILBERT, F. and D.V. HELMBERGER (1972): Generalized ray theory for a layered sphere, *Geophys. J. R. Astron. Soc.*, **27**, 57-80.

GRAND, S.P. and D.V. HELMBERGER (1984): Upper mantle shear structure of North America, *Geophys. J. R. Astron. Soc.*, **76**, 399-438.

GRAVES, R.W. and D.V. HELMBERGER (1988): Upper mantle cross section from Tonga to Newfoundland, *J. Geophys. Res.*, **93**, 4701-4711.

HELMBERGER, D.V. (1968): The crust-mantle transition in the Bering Sea, *Bull. Seismol. Soc. Am.*, **58**, 179-214.

HELMBERGER, D.V. (1983): Theory and application of synthetic seismograms, *Earthquakes: Observation*, Theory and Interpretation, *LXXXV Corso*.

HELMBERGER, D.V., G. ENGEN and S.P. GRAND (1985): Notes on wave propagation in laterally varying structure, *J. Geophys.*, **58**, 82-91.

HELMBERGER, D.V. and J. VIDALE (1988): Modeling strong motions produced by earthquakes with two-dimensional numerical codes, *Bull. Seism. Soc. Am.*, **78**, 109-121.

HONG, T.L. and D.V. HELMBERGER (1978): Glorified optics and wave propagation in nonplanar structure, *Bull. Seismol. Soc. Am.*, **68**, 1313-1330.

KENDALL, J.M. and P.M. SHEARER (1993): Lateral variations in D″ thickness from long-period shear-wave data, *J. Geophys. Res.*, **99**, 11575-11590.

KIND, R. and G. MÜLLER (1975): Computations of SV waves in realistic Earth models, *J. Geophys.*, **41**, 149-172.

LAY, T. and D.V. HELMBERGER (1983): The shear wave velocity gradient at the base of the mantle, *J. Geophys. Res.*, **88**, 8160-8170.

MASTERS, T.G., H. BOLTON and P.M. SHEARER (1992): Large-scale 3 dimensional structure of the mantle (abstract), *EOS, Trans.* AGU., **73**, 201.

MITCHELL, B.J. and D.V. HELMBERGER (1973): Shear velocities at the base of the mantle from observations of S and ScS, *J. Geophys. Res.*, **78**, 6009-6020.

RICHARDS, P.G., D.C. WITTE and G. EKSTROM (1991): Generalized ray theory for seismic waves in structures with planar nonparalleled interfaces, *Bull. Seism. Soc. Am.*, **81**, 1309-1331.

SILVER, P. and C.R. BINA (1993): An anomaly in the amplitude ratio of SKKS/SKS in the range 100-108° from portable teleseismic data, *Geophys. Res. Lett.* (in press).

SIPKIN, S.A. and T.H. JORDAN (1980): Multiple ScS travel times in the Western Pacific: Implications for mantle heterogeneity, *J. Geophys. Res.*, **85**, 853-861.

STEAD, R.J. and D.V. HELMBERGER (1988): Numerical-analytical interfacing in two-dimensions with applications to modeling NTS seismograms, *PAGEOPH*, **128**, 157-193.

SU, W.J. and A.M. DZIEWONSKI (1994): Degree 12 model of shear velocity heterogeneity in the mantle, *J. Geophys. Res.*, **99**, 6945-6980.

TANIMOTO, T. (1990): Long-wavelength *S*-wave velocity structure throughout the mantle, *Geophys. J. Int.*, **100**, 327-336.

VIDALE, J., D.V. HELMBERGER and R.W. CLAYTON (1985): Finite-difference seismograms for SH-waves. *Bull. Seism. Soc. Am.*, **75**, 1765-1782.

WEBER, M. and J.P. DAVIS (1990): Evidence of a laterally variable lower mantle structure from *P*- and *S*-waves, *Geophys. J. Int.*, **102**, 231-255.

WIGGINS, R.A. (1976): Body wave amplitude calculations, II, *Geophys. J. R. Astron. Soc.*, **46**, 1-10.

WIGGINS, R.A. and J.A. MADRID (1974): Body wave amplitude calculations, *Geophys. J. R. Astron. Soc.*, **37**, 423-433.

YOUNG, C.J. and T. LAY (1987): Evidence for a shear velocity discontinuity in the lower mantle beneath India and the Indian Ocean, *Phys. Earth Planet. Inter.*, **49**, 37-53.

ZHANG, J. and T. LAY (1984): Investigation of a lower mantle shear wave triplication using broadband array, *Geophys. Res. Lett.*, **11**, 620-623.